

Hydrodynamical models and synthetic spectra of circumstellar dust shells around AGB stars

II. Time-dependent simulations

Matthias Steffen^{1,2}, Ryszard Szczerba³, and Detlef Schönberner⁴

¹ Astrophysikalisches Institut Potsdam, D-14482 Potsdam, Germany (MSteffen@aip.de)

² Institut für Astronomie und Astrophysik der Universität Kiel, D-24098 Kiel, Germany (Steffen@astrophysik.uni-kiel.de)

³ Nicolaus Copernicus Astronomical Center, PL-87-100 Torun, Poland (Szczerba@ncac.torun.pl)

⁴ Astrophysikalisches Institut Potsdam, D-14482 Potsdam, Germany (Deschoenberner@aip.de)

Received 19 February 1998 / Accepted 19 May 1998

Abstract. We have employed time-dependent two-component hydrodynamics/radiative transfer calculations to investigate the structure, dynamics and emergent spectral energy distribution of dusty circumstellar shells around carbon and oxygen stars in the final stages of their AGB evolution. These internally consistent, physical models describe a stellar wind driven by radiation pressure on dust grains and subsequent momentum transfer to the gas component via collisions. Detailed stellar evolution calculations, with a prescribed mass loss rate that is a function of the fundamental stellar parameters, have been used as a time-dependent inner boundary condition for the numerical solution of the coupled equations of hydrodynamics and frequency-dependent radiative transfer governing the structure and temporal evolution of the circumstellar dust/gas shell.

The calculations are based on one particular evolutionary track for an initial stellar mass $M_i = 3.0 M_\odot$ and a final mass $M_f = 0.605 M_\odot$, but for different assumptions concerning the composition of the dust grains: amorphous carbon or “astromical” silicates. Using our hydrodynamics code to simulate the dynamical response of the circumstellar wind shell to the evolutionary changes of the stellar parameters, we find that the large temporal variations of stellar luminosity and mass loss rate associated with the final thermal pulses near the end of the AGB evolution lead to characteristic, time-dependent signatures in the density structure and emergent energy distribution of the circumstellar dust shell. We present the resulting “loops” in the IRAS two-color-diagram, which we find to extend to regions quite remote from the simple color-color relation defined by steady state models.

These time-dependent hydrodynamical models explain the existence of carbon and oxygen stars with excess emission near λ 60 and $100 \mu\text{m}$ as a natural consequence of the sharp decrease of the mass loss rate following a thermal pulse, leading to the development of a *detached dust shell*. As an illustration, we present a series of synthetic spectra and corresponding $100 \mu\text{m}$ surface brightness distributions showing the time-evolution of

the circumstellar dust emission during a thermal pulse cycle, both for a carbon-rich and an oxygen-rich dust shell.

We demonstrate that it is unrealistic to assume a fixed velocity profile which is independent of mass loss rate: to a first approximation, the gas velocity is a bimodal function of the mass loss rate. A short event of high mass loss does *not* simply translate into a correspondingly narrow, high-density shell moving through the circumstellar envelope. Rather, the signature of a short mass loss peak broadens due to velocity gradients as it moves towards the outer regions of the wind. Hence, this is hardly a viable scenario to explain the existence of very thin molecular shells that have recently been detected around some carbon stars. Our simulations suggest a more promising mechanism producing thin shells of enhanced gas density in the outer regions of carbon-rich AGB shells: interaction of winds of different speed and density.

Key words: stars: AGB and post-AGB – circumstellar matter – stars: Mass loss – dust, extinction – hydrodynamics – radiative transfer

1. Introduction

Before turning into planetary nebulae, low to intermediate mass stars ($1-8 M_\odot$) are found to evolve along the Asymptotic Giant Branch (AGB). In this phase, mass loss dominates over nuclear burning and finally terminates the AGB evolution by reducing the mass of the stellar envelope below some critical limit. High mass loss rates between 10^{-6} and $10^{-4} M_\odot \text{yr}^{-1}$ are very often detected, mostly by excess continuum radiation in the infrared, originating from thermal emission of circumstellar dust (e.g. Herman et al. 1986; Jura 1987; Bedijn 1987; Schutte & Tielens 1989), and by the presence of molecular rotation lines from different molecules seen in emission at submm, mm, and cm wavelengths (e.g. Knapp & Morris 1985; Netzer & Knapp 1987).

It is now generally accepted that the mechanism responsible for such high mass loss rates during the AGB evolution is based on the efficiency of radiation pressure on dust grains. Shock waves generated by Mira-type stellar pulsations are essential for accelerating the outflow from the stellar surface to the sonic point where the gas becomes cool enough at sufficiently high densities to allow heavy elements to condense as grains. The dust grains belong to one of two different types: (1) silicate-type grains, found around so called “oxygen stars” with an abundance ratio $C/O < 1$, and (2) carbon-based grains around “carbon stars” with $C/O > 1$. These dust particles efficiently scatter and absorb photons, extracting momentum and energy from the stellar radiation field. The acquired momentum is transferred to the gas by collisions between dust particles and gas molecules (see e.g. Gilman 1972; Salpeter 1974; Kwok 1975; Goldreich & Scoville 1976), while the absorbed energy is re-radiated at infrared wavelengths.

Up to now, *hydrodynamical* models of dust driven winds on the AGB do *not* generally include the “long-term” variations of the stellar parameters and mass loss rate (on stellar evolution time scales of the order of 10^3 to 10^5 years, as opposed to stellar radial pulsation time scales of several 100 days), although it is well known that the stellar luminosity and (very likely) the mass loss rate undergo significant variations when so-called “thermal pulses” occur on the upper AGB (e.g. Iben & Renzini 1983).

In fact, recent observations have clearly revealed the existence of so called “detached shells” around a number of AGB stars, which has been taken as strong evidence that mass loss may be temporarily interrupted (e.g. Willems & de Jong 1988; Chan & Kwok 1988; Zijlstra et al. 1992; Olofsson et al. 1996; Izumiura et al. 1996, 1997). However, the exact evolutionary behavior of the mass loss remains unknown. Two general scenarios have been proposed that relate mass loss interruptions to the rapid luminosity variations occurring when AGB stars undergo a thermal pulse cycle. Both of them are based on the observation that all carbon stars with excess emission at $\lambda 60 \mu\text{m}$ are optically visible. In the first scenario (favored by e.g. Zuckerman 1993 or Olofsson et al. 1996) the far infrared excess is explained by a rather low steady mass loss, only interrupted by a short high mass loss peak, possibly caused by a thermal pulse. In the second one (e.g. van der Veen & Habing 1988; Egan et al. 1996) a quite long period of high mass loss followed by a phase of greatly reduced mass loss in the aftermath of a thermal pulse produces a detached shell and corresponding excess emission, provided that the mass loss minimum lasts long enough to allow for sufficient expansion and cooling of the dust shell before the high mass loss resumes and obscures the star again. In the former case it seems that the mass loss “pulse” does not last long enough to create a detached dust shell containing enough matter to account for the observed emission at long wavelengths (Egan et al. 1996), a conclusion supported by the present work.

From the theoretical side, it is presently not possible to derive mass loss rates along the AGB from first principles (except for some very cool, high luminosity carbon stars; see Dominik et al. 1990, Arndt et al. 1997). Existing stellar evolution calculations resort to semi-empirical mass loss prescriptions (Vassiliadis & Wood 1993; Blöcker 1995), which, due to the occurrence of thermal pulses, lead to considerable variations of the mass loss rate on time scales which are short compared to the flight time of a gas parcel through the circumstellar envelope. Hence, the situation is far from steady state and time-dependent hydrodynamics/radiative transfer calculations taking into account the “long-term” effects of stellar evolution are needed for a physically consistent interpretation of the observed spectral energy and surface brightness distributions of mass losing AGB stars. This is particularly important for understanding the formation and structure of multiple shells, revealing part of the previous mass loss history. Ultimately, analysis of the observed properties of the circumstellar shells of a large number of AGB stars should allow to check the presently adopted mass loss laws and, if necessary, to derive empirical corrections.

A first brief report of time-dependent hydrodynamical wind calculations similar to those presented here was given by Vassiliadis & Wood (1992), who used a simple one-component hydrodynamics code (Wood 1979) ignoring the details of dust radiative transfer. The circumstellar density and velocity structures they find seem to be very similar to those obtained in the present work. However, Vassiliadis & Wood (1992) did not compute the emergent spectral energy distribution for a comparison with observations.

We have developed a new code which is suitable to treat the *time-dependent two-component radiation hydrodynamics* problem of dust driven stellar outflows in spherical symmetry. The code includes a detailed solution of frequency-dependent radiative transfer in the dust component and provides synthetic emergent spectra. It is designed to take into account the evolutionary changes of the stellar parameters and the resulting variable mass loss rate through a time-dependent inner boundary condition for the system of partial differential equations describing the model of the circumstellar shell. In a previous paper (Steffen et al. 1997a, henceforth Paper I), we have tested this code and have used it to study the hydrodynamical properties and spectral energy distributions of *steady state* solutions for a variety of different parameters. In the present work we apply the code to the *time-dependent* case, elaborating on preliminary investigations published before (Szczerba & Marten 1993; Schönberner et al. 1997, 1998; Steffen et al. 1997b; Steffen & Szczerba 1997).

In Sect. 2 we describe the modifications (relative to the equations given in Paper I) and additional assumptions incorporated into our code for the treatment of the time-dependent case. The input data taken from stellar evolution calculations with mass loss (Blöcker, 1995) are briefly discussed in Sect. 3, while the main results of our computations for one particular evolutionary track, but assuming different dust properties, are presented in Sect. 4. In Sect. 5, we compare the observed distribution of AGB objects in the IRAS two-color-diagram with the color evolution computed from our dynamical models, and show that the observed spectral energy distribution of the prominent carbon star S Scuti (Groenewegen & de Jong 1994; Olofsson et al. 1996) and the detached dust shell of the another well-known carbon star, Y CVn, (Izumiura et al. 1996) are explained in a natural way by our models, as is the rapid transition to the post-AGB

is the rapid transition to the post-AGB

phase. Finally, in Sect. 6, we summarize the main conclusions of this work and close with some remarks on possible future improvements of the AGB winds models.

2. Time-dependent hydrodynamical model calculations

Our model calculations are based on the following assumptions: The central AGB star's luminosity, $L_*(t)$, effective temperature, $T_{\text{eff}}(t)$, and mass loss rate, $\dot{M}(t)$, vary as a function of time according to the stellar evolution calculations by Blöcker (1995). The mass of the star, $M_*(t)$, changes in agreement with the prescribed mass loss rate ($dM_*/dt = -\dot{M}$; note that \dot{M} is defined here as a positive quantity). The evolutionary track used for the examples presented in the following is for a star with an initial mass $M_i = 3.0 M_\odot$ which, due to mass loss, is reduced to a final mass $M_f = 0.605 M_\odot$ when the end of the AGB is reached.

At some distance from the star the outflowing gas has cooled to the dust condensation temperature (T_{cond}) and dust is assumed to form instantly at this radius $r_1(t)$, which must very closely coincide with the sonic point (critical point). Since at a given distance from the star the dust temperature is a function of L_* , T_{eff} , and \dot{M} , the location of the dust formation point r_1 can vary considerably over a thermal pulse cycle on the upper AGB, typically by a factor of 2. After their formation the dust grains of single size are accelerated away from the central star by radiation pressure, drift through the gas and drag along the gas component due to the frictional coupling provided by dust-gas collisions.

A radiation hydrodynamics code, originally developed to investigate the dynamical evolution of protostellar clouds, is employed to solve the time-dependent equations of hydrodynamics and frequency-dependent radiative transfer for a two-component 'fluid' consisting of *gas* and *dust* under the assumption of spherical symmetry. Details about the numerical methods used are described by Yorke & Krügel (1977), and by Yorke (1980a; 1980b). The code has been modified extensively to adapt it for the modeling of dusty stellar outflows. A *moving grid* is employed to keep the dust formation point close to the innermost point of the numerical mesh. The basic equations to be solved in this context are given below.

2.1. Equations of radiation hydrodynamics

The structure and time evolution of the stellar outflow is governed by the following set of partial differential equations (basic equations of hydrodynamics):

Equation of motion for the gas component:

$$\frac{\partial u}{\partial t} + (u - v_{\text{grid}}) \frac{\partial u}{\partial r} = -\frac{1}{\rho} \frac{\partial p}{\partial r} - \frac{GM_r}{r^2} + n_d \pi a^2 (w - u) \sqrt{\bar{v}^2 + (w - u)^2} + g_{\text{shock}}, \quad (1)$$

where u and w are the gas and the dust velocity (relative to the central star), respectively, v_{grid} is the radial velocity of the moving grid, ρ is the gas density, p is the gas pressure, M_r

is the total mass inside radial coordinate r , $\bar{v} = \sqrt{8RT/\pi\mu}$ measures the thermal velocity dispersion of the gas particles at temperature T (for the molecular weight we assumed $\mu \approx 1.3$, corresponding to gas of solar composition with hydrogen in atomic form; the choice of μ is not critical, see Paper I) and g_{shock} is discussed below. Note that $\frac{\partial f}{\partial t}$ means the time derivative of f at a fixed position of the moving grid. All other symbols have their usual meaning. The first term on the right hand side describes the acceleration due to the gas pressure gradient (gas pressure term), the second term corresponds to the gravitational force and the third term accounts for the dynamical coupling between gas and dust (friction term).

The last term, g_{shock} , is our simplistic approach to represent the time-averaged outward acceleration of the gas due to shock waves generated by the Mira-type pulsations of the central AGB star. It is introduced as an artificial acceleration term supporting the outflow, designed to ensure that the gas velocity u cannot drop significantly below a minimum velocity u_a . On the other hand, we require g_{shock} to vanish whenever the gas outflow velocity u exceeds the limit u_b . The free parameters u_a and u_b ($u_a < u_b$) control the magnitude and range of g_{shock} . The values adopted here for u_a and u_b are $u_a = 3$ km/s and $u_b = 4$ km/s ($u_a = u_1$, see Sect. 2.5).

We have constructed the following analytical expression for g_{shock} :

$$g_{\text{shock}} = \frac{GM_r}{r^2} g_1(u) g_2(r), \quad (2)$$

where

$$g_1(u) = \begin{cases} \left(\frac{u_b - u}{u_b - u_a}\right)^3 & \text{if } u < u_b \\ 0 & \text{otherwise} \end{cases} \quad (3)$$

and

$$g_2(r) = \begin{cases} 1 & \text{if } 2v_{\text{esc}} > u_b \\ \left(\frac{2v_{\text{esc}} - u_a}{u_b - u_a}\right) & \text{if } u_a \leq 2v_{\text{esc}} \leq u_b \\ 0 & \text{if } 2v_{\text{esc}} < u_a \end{cases} \quad (4)$$

Here

$$v_{\text{esc}} = \sqrt{\frac{2GM_r}{r}} \quad (5)$$

is the local escape velocity at distance r from the star. Notice that there is no particular physical model behind the analytical form of g_{shock} .

Evidently, $g_1(u_a) = 1$, so g_{shock} just balances the gravitational attraction if the gas velocity equals u_a at least in the inner region, $r \leq r_a$, where $v_{\text{esc}} > u_b/2$ and the second factor $g_2(r) \equiv 1$. The factor $g_2(r)$ was introduced to ensure that g_{shock} vanishes in the outer part of the shell, $r \geq r_b$, where $v_{\text{esc}} < u_a/2$, irrespective of the actual gas velocity u . For a stellar mass of $M_r = 2M_\odot$ our choice of u_a and u_b gives $r_a \approx 1.3 \cdot 10^{16}$ cm and $r_b \approx 2.4 \cdot 10^{16}$ cm. It can be shown that for these parameters the terminal outflow velocity will always be larger than $0.8 u_a$.

In simulations performed with $g_{\text{shock}} \equiv 0$, we sometimes found conditions where the net acceleration of the gas was negative due to the weak coupling between gas and dust during periods of low mass loss, resulting in a gas flow back towards the star (the same behavior was also found by Vassiliadis & Wood 1992). Such situations cannot (presently) be handled in a self-consistent way by our code and lead to unrealistic density structures. We circumvented these problems by introducing g_{shock} .

Equation of continuity for the gas component:

$$\frac{\partial \rho}{\partial t} + \frac{1}{r^2} \frac{\partial}{\partial r} (r^2 \rho u) = v_{\text{grid}} \frac{\partial \rho}{\partial r} \quad (6)$$

In addition to the usual terms on the left hand side, the term on the right hand side describes the change of the gas density (as seen by an observer attached to the moving grid) due to the grid motion relative to the density distribution in the inertial frame of reference.

Equation of motion for the dust component (single grain):

$$\frac{\partial w}{\partial t} + (w - v_{\text{grid}}) \frac{\partial w}{\partial r} = \frac{\bar{C}_{\text{ext}}^{\text{F}} L_{*}}{m_{\text{d}} 4\pi r^2 c} - \frac{GM_{\text{r}}}{r^2} - \frac{\rho}{m_{\text{d}}} \pi a^2 (w - u) \sqrt{v^2 + (w - u)^2}, \quad (7)$$

where m_{d} and a are the mass and radius of a dust grain, respectively, c is the speed of light, and

$$\bar{C}_{\text{ext}}^{\text{F}} = \int_0^{\infty} C_{\text{ext}}(\nu) F(\nu) d\nu / \int_0^{\infty} F(\nu) d\nu \quad (8)$$

is the flux weighted extinction cross section (including absorption and isotropic scattering: $C_{\text{ext}}(\nu) = C_{\text{abs}}(\nu) + C_{\text{sca}}(\nu)$). The first term on the right hand side of Eq. 7 describes the acceleration of a dust grain by radiation pressure, the second term corresponds to the gravitational deceleration by the central mass (usually much smaller than the radiative acceleration), and the third term again accounts for the dynamical coupling between gas and dust. Interaction between dust particles (“dust pressure”) and the effect of shock waves on dust are neglected.

Equation of continuity for the dust component:

$$\frac{\partial n_{\text{d}}}{\partial t} + \frac{1}{r^2} \frac{\partial}{\partial r} (r^2 n_{\text{d}} w) = v_{\text{grid}} \frac{\partial n_{\text{d}}}{\partial r}, \quad (9)$$

where n_{d} is the number density of dust grains. Hence, the total amount of dust in the computational domain is given by the fluxes through the model boundaries. Condensation or evaporation of dust is not considered.

For a given dust density distribution, the thermal structure of the dust shell is determined by the radiation field of the central star, which, for simplicity, is assumed to radiate as a blackbody with $T_{\text{BB}} = T_{\text{eff}}$. The energy equation for the dust component stipulates the condition of radiative equilibrium at any time:

Energy Equation for the dust component:

$$\frac{1}{r^2} \frac{\partial}{\partial r} (r^2 F_{\text{rad}}) = 0 \quad (10)$$

where F_{rad} is the frequency-integrated radiative energy flux. The temperature of the dust component is related to the equilibrium radiation field by

$$\int_0^{\infty} C_{\text{abs}}(\nu) J_{\nu} d\nu = \int_0^{\infty} C_{\text{abs}}(\nu) B_{\nu}(T_{\text{d}}) d\nu \quad (11)$$

where J_{ν} is the angle-averaged specific intensity and B_{ν} is the Planck function at the local dust temperature T_{d} . Note that J_{ν} does not only represent the direct stellar radiation but also includes the thermal emission and diffuse scattered radiation from the dust shell. Details about the method used for the numerical solution of the equation of radiative transfer in spherical geometry are given in Paper I and in Yorke (1980b).

We presently do not solve the energy equation for the gas component. Instead, we simply take

Energy Equation for the gas component:

$$T = T_{\text{d}}, \quad (12)$$

an assumption which needs to be modified for applications where the gas temperature is a critical quantity (e.g. for the calculation of molecular emission line profiles).

Finally, we would like to point out that the numerical scheme employed for the solution of the hydrodynamical equations is fully implicit. This means that the time step of the simulations is *not* restricted to the Courant time step. This is a very important advantage in the present application where it is necessary to cover long time intervals.

2.2. Dust opacities

The solution of the set of equations given above depends on the geometrical and optical properties of the dust grains and their abundance. In this study we use “*astronomical*” silicates or *amorphous carbon*, with properties as specified in Table 1 (see also Fig. 1 of Paper I). The corresponding opacity data for “*astronomical*” silicates were kindly provided by B. Draine (for details see Laor & Draine 1993), and were taken from Rouleau & Martin (1991) in the case of amorphous carbon. In the hydrodynamical calculations we use a grid of 169 wavelength points distributed unevenly between 0.01 and 3100 μm .

2.3. Initial condition, radial grid

The time-dependent simulations start from a steady state solution (see Paper I) computed for the stellar parameters and mass loss rate corresponding to the initial time t_0 . The distance of the inner edge of the *dust* shell from the central star, r_{cond} , is given by the condition

$$T_{\text{d}}(r_{\text{cond}}) = T_{\text{cond}} \quad (13)$$

Table 1. Dust grain properties and abundances used in this work. The corresponding optical properties are shown in Fig. 1 of Paper I.

	Astronomical Silicates	Amorphous Carbon
Grain size [μm]	0.05	0.05
Specific mass density ρ_i [g cm^{-3}]	3.30	1.85
Condensation temperature [K]	800	1300
Dust-to-gas ratio $\delta = \rho_d / \rho$	0.0050	0.0015

where T_{cond} is the dust condensation temperature (see Table 1) and $T_d(r)$ given through Eq. 11. For the initial model, the computational radial grid starts at $r_1(t_0) = r_{\text{cond}}$, the inner edge of the dust shell, and ends at an outer radius $r_{\text{out}}(t_0) = 3 \cdot 10^{18}$ cm (≈ 1 pc). All models used for this investigation have $N = 480$ radial grid point spaced according to

$$r_i = r_1 + (r_N - r_1) \frac{q^{i-1} - 1}{q^{N-1} - 1}; \quad i = 1, N. \quad (14)$$

By choosing an appropriate value $q > 1$ we have concentrated the grid points in the inner part of the model such that the spatial resolution in the innermost parts (acceleration region) is four times better than for an equidistant logarithmic grid covering the same radius range with the same number of points.

In order to take into account the presence of the *interstellar medium* (ISM), we modified the initial steady state solution in the outer parts where the gas density drops below $\rho_{\text{ISM}} = 10^{-23}$ g cm $^{-3}$. Here we require $\rho \equiv \rho_{\text{ISM}}$, $\rho_d \equiv \delta \rho_{\text{ISM}}$, and $u \equiv w \equiv 0$. An example of an initial velocity and density structure, including ISM, is shown in Fig. 3 (left hand panels). The role of the ISM is further discussed in Sect. 4.1.1.

2.4. Controlling the grid motion

Since the stellar parameters and the mass loss rate change with time, the position of the dust condensation radius, r_{cond} , will follow these variations.

Our calculations employ a grid that moves with a time-dependent velocity, $v_{\text{grid}}(t)$, relative to the central star such that

$$r_1(t) \approx r_{\text{cond}}(t). \quad (15)$$

The grid velocity is uniform throughout the grid, i.e. v_{grid} is independent of r and the initial distribution of grid points given by Eq. 14 is only translated as a whole. Based on the approximation $rT^2 \approx \text{const}$, i.e. $\delta r/r = 2\delta T/T$, v_{grid} is computed as

$$v_{\text{grid}}(t) = 2 \frac{r_1(t)}{\tau_{\text{grid}}} \left(\frac{T_d(r_1(t))}{T_{\text{cond}}} - 1 \right). \quad (16)$$

The time constant τ_{grid} controls the response time of the grid motion to changes of the dust condensation radius. If r_{cond}

changes on time scales much longer than τ_{grid} , the moving grid can closely follow the position of the dust condensation radius. Variations on time scales much shorter than τ_{grid} are essentially ignored. We have chosen $\tau_{\text{grid}} = 500$ yrs, corresponding to the shortest time scales encountered in the variations of the stellar parameters during a thermal pulse. This choice also ensures that the resulting grid velocities are always small compared to the gas outflow velocities. If necessary, the hydrodynamical time step, Δt , is reduced to restrict the grid motion over Δt to be always less than the distance between any two adjacent grid points.

The alternative to employing a moving grid is to use a fixed grid which is large enough to cover the whole range of possible dust condensation radii. In this case one would have to deal with more or less extended dust-free regions in the inner parts of the computational domain, requiring special treatment. This complication is avoided in the moving grid approach, which we found to be more economic (in terms of the number of grid points required) and more straightforward.

2.5. Boundary conditions

The boundary conditions at r_1 essentially determine the nature of the solution. At the *moving inner boundary* we adopt a constant initial velocity which is identical for the gas and the dust component and is taken to be 3 km/s, close to (but not smaller than) the local isothermal sound speed:

$$u_1 \equiv u(r_1) = w(r_1) = 3 \text{ km/s} \approx c_s(T_{\text{cond}}) \quad (17)$$

The gas density at the inner boundary is then given by

$$\rho(r_1)(t) = \frac{\dot{M}(t)}{4\pi r_1^2(t) u_1}. \quad (18)$$

The mass loss rate as a function of time through the inner boundary of the dust shell, $\dot{M}(t)$, may, in principle, be specified in an arbitrary way. In this work it is enforced in accordance with a particular stellar evolution sequence as described below. The dust density is related to the gas density via the dust-to gas ratio δ as

$$\rho_d(r_1)(t) = \delta f_{\text{cond}}(\dot{M}) \rho(r_1)(t). \quad (19)$$

The function $f_{\text{cond}}(\dot{M})$ controls the degree of dust condensation and is defined as

$$\log f_{\text{cond}}(x) = \begin{cases} -2 & \text{if } x \leq 0 \\ -2(2x^3 - 3x^2 + 1) & \text{if } 0 < x < 1 \\ 0 & \text{if } x \geq 1 \end{cases} \quad (20)$$

where

$$x = \frac{\log(\dot{M}/\dot{M}_1)}{\log(\dot{M}_2/\dot{M}_1)} \quad (21)$$

with $\dot{M}_1 = 10^{-7} M_{\odot} \text{ yr}^{-1}$ and $\dot{M}_2 = 3 \cdot 10^{-7} M_{\odot} \text{ yr}^{-1}$. This means that we assume the process of dust condensation to become inefficient below mass loss rates of $\dot{M} \approx$

$3 \cdot 10^{-7} M_{\odot} \text{ yr}^{-1}$, which via Eq. 18 may be translated into a critical gas density of $\rho_0 \approx 5 \cdot 10^{-16} \text{ g cm}^{-3}$.

Although, due to the finite value of the time constant τ_{grid} , the actual dust temperature at the innermost grid point can deviate somewhat from T_{cond} , it is assumed that dust condensation, and hence dust acceleration, always begins at $r_1(t)$.

For the computation of the radiative transfer, we apply a time-dependent *stellar* radiation field at the inner boundary of the dust shell, with a spectral energy distribution corresponding to that of a blackbody at $T_{\text{BB}}(\text{star}) = T_{\text{eff}}(t)$, and with a net radiative flux given by

$$F(\text{star}) = \frac{L_*(t)}{4\pi r_1^2(t)} \quad (22)$$

At the outer boundary, $u(t)$, $w(t)$, $\rho(t)$ and $\rho_d(t)$ can be computed consistently from the hydrodynamical equations in the case of a *supersonic* outflow considered here. We assume an external, isotropic (“interstellar”) radiation field to be incident on the outer boundary, characterized by a blackbody temperature $T_{\text{BB}}(\text{external}) = 3 \text{ K}$.

3. Stellar evolution with mass loss

For a complete definition of the problem, we finally have to specify the basic properties of the central star as a function of time. These are $L_*(t)$, $T_{\text{eff}}(t)$, which together define the stellar radius $R_*(t)$, and $M(t)$. The mass of the central star, $M_*(t)$, then changes in accordance with the mass loss rate.

For the solar-composition stellar model adopted as a typical example in this work, the changes of the stellar parameters during the different stages of evolution, from the main sequence through the red giant branch, the asymptotic giant branch, the planetary nebula phase and finally towards the White Dwarf regime, are illustrated in the corresponding Hertzsprung-Russell-Diagram in the upper panel of Fig. 1.

According to stellar evolution calculations with mass loss by Blöcker (1995), this model suffers a total of 17 helium shell flashes (thermal pulses) on the so-called “thermally pulsing AGB” (TP-AGB) and loses about 80% of its initial mass during this stage. The end of AGB evolution and transition to the phase of a proto-planetary nebula (PPN) is signaled by a rapid increase of T_{eff} at constant L_* . After a few thousand years the star will be found at the center of a planetary nebula (PN). When the nuclear energy generation ceases at $T_{\text{eff}} \gtrsim 100\,000 \text{ K}$, the luminosity begins to drop and the star eventually cools into the White Dwarf (WD) regime.

In the context of the hydrodynamical simulations of the circumstellar gas/dust shell described in the remainder of this work, we will only consider the final phases of evolution on the TP-AGB, covering the last four thermal pulses (number 14 to 17, cf. lower panel of Fig. 1). For the sake of simplicity we will henceforth refer to pulses number 14, 15, 16 and 17 as the ‘first’, ‘second’, ‘third’ and ‘fourth’ (or final) thermal pulse, respectively.

The temporal evolution of *luminosity*, *effective temperature*, *mass loss rate* and *stellar mass* during the last 350 000 years on

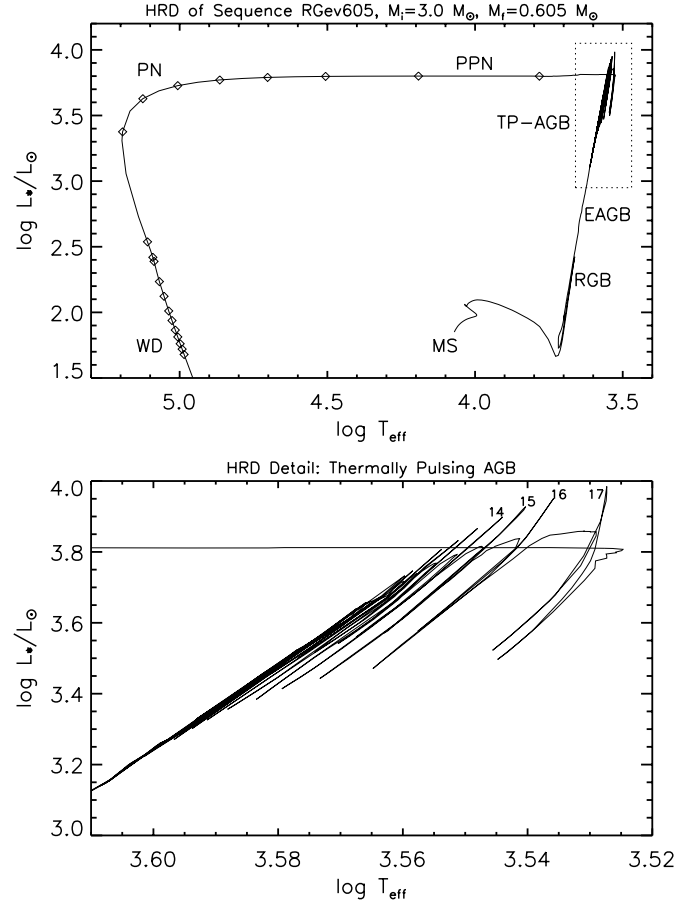


Fig. 1. Top: Evolutionary track of a stellar model with an initial mass of $3 M_{\odot}$ in the Hertzsprung-Russell-Diagram according to stellar evolution calculations with mass loss by Blöcker (1995). This diagram covers the basic stages of evolution, from the main sequence (MS) through the red giant branch (RGB), the early AGB (EAGB), the so-called “thermally pulsing AGB” (TP-AGB, boxed region at upper right) and finally the proto-planetary nebula (PPN) and planetary nebula (PN) phases leading towards the White Dwarf (WD) regime. Open diamonds are plotted in time intervals of 1000 yrs (beginning at $t = 0$ yrs) for the first 10 000 yrs of post-AGB evolution, and in time intervals of 10 000 yrs thereafter. **Bottom:** Close-up view of the “thermally pulsing AGB”. During this phase of evolution, the model suffers a total of 17 helium shell flashes (thermal pulses) over a period of about $1.5 \cdot 10^6$ yrs and loses about 80% of its initial mass. The final four thermal pulses are labeled “14” - “17”.

the AGB and the following few thousand years of the post-AGB evolution is plotted in Fig. 2. The final thermal pulses on the AGB recur on a typical interpulse time scale of roughly 90 000 yrs.

In the corresponding stellar evolution calculations the effect of mass loss on the stellar evolution is taken into account through a parameterized mass loss description:

$$\dot{M} = 4.38 \cdot 10^{-9} M_*^{-2.1} L_*^{2.7} \dot{M}_{\text{R}} \quad [M_{\odot} \text{ yr}^{-1}], \quad (23)$$

where the Reimers (1975) mass loss rate is

$$\dot{M}_{\text{R}} = 4 \cdot 10^{-13} \frac{L_* R_*}{M_*} \quad [M_{\odot} \text{ yr}^{-1}]. \quad (24)$$

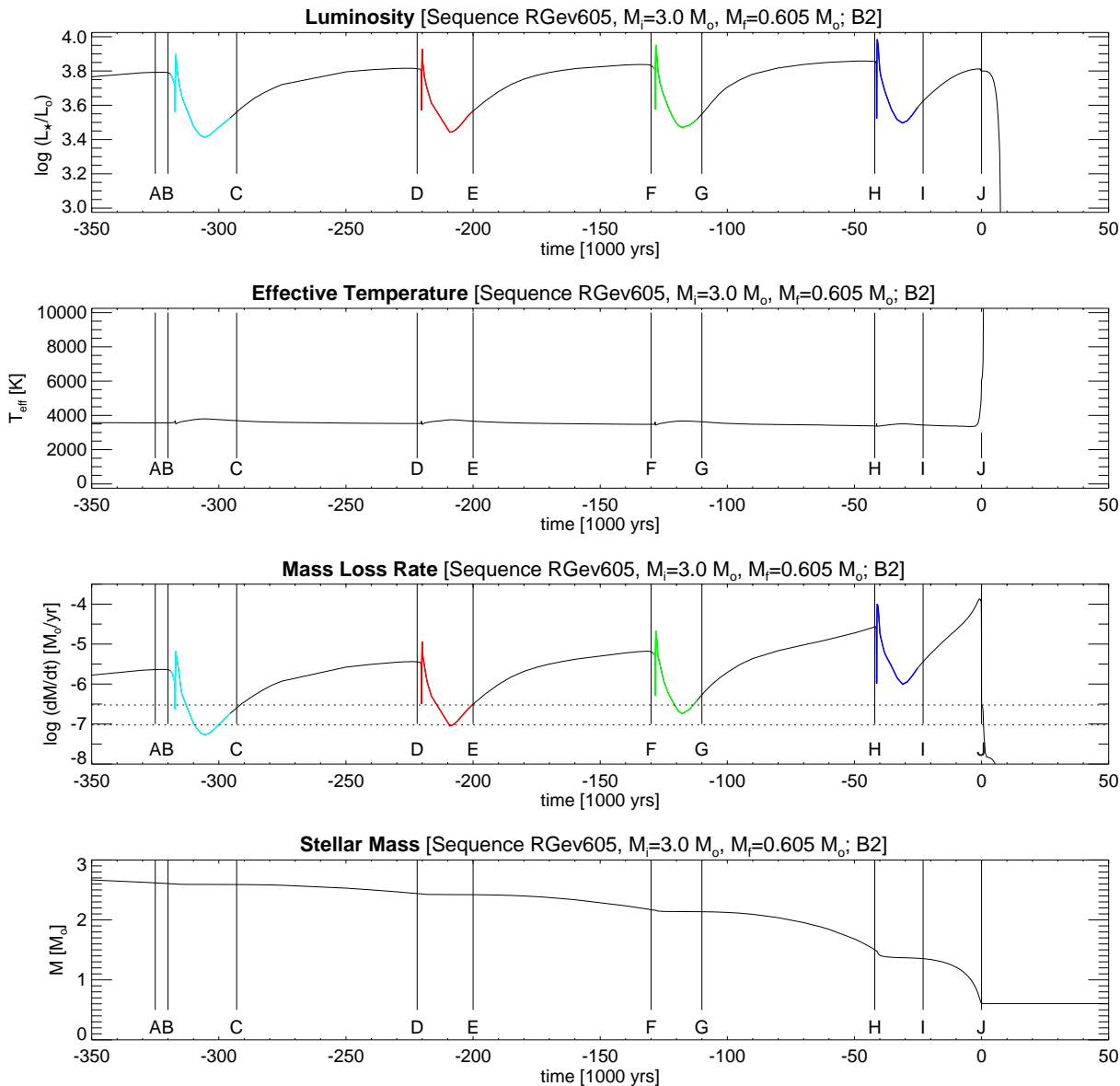


Fig. 2. Stellar luminosity, effective temperature, mass loss rate and mass (from top to bottom) vs. time for a $3 M_{\odot}$ model sequence after Blöcker (1995), including the final four thermal-pulse cycles on the AGB (negative times). For mass loss rates between the dotted horizontal lines (middle frame), the dust condensation fraction is assumed to drop smoothly by a factor of 100 (see Eq. 20). At time zero the stellar effective temperature rises sharply (see second panel), marking the beginning of the model’s post-AGB evolution. Labels A to J are referred to in the text. For details of $\dot{M}(t)$ see also Figs. 10 and 19

This mass loss formula (Eq. 23) is based on hydrodynamical calculations of shock-driven winds in the atmospheres of long-period Mira-like stars by Bowen (1988), taking into account radiation pressure on dust in a schematic way. The resulting AGB mass loss rates dramatically increase with the stellar luminosity. As a consequence, most of the mass is lost during the last few thermal pulses before the end of the AGB evolution (cf. lower panel of Fig. 2). In our example, the initial mass of $3M_{\odot}$ is reduced to a final mass of $0.605M_{\odot}$.

4. Results of the numerical simulations

4.1. Time evolution of a circumstellar shell with amorphous carbon dust - a paradigmatic overview

The example results presented in the following are based on the stellar evolution sequence described in the previous section. The data shown in Fig. 2 are used as a time-dependent inner boundary condition for the hydrodynamical simulation of the long-term evolution of the circumstellar gas/dust shell as explained in Sect. 2.5. The dust is assumed to condense as grains

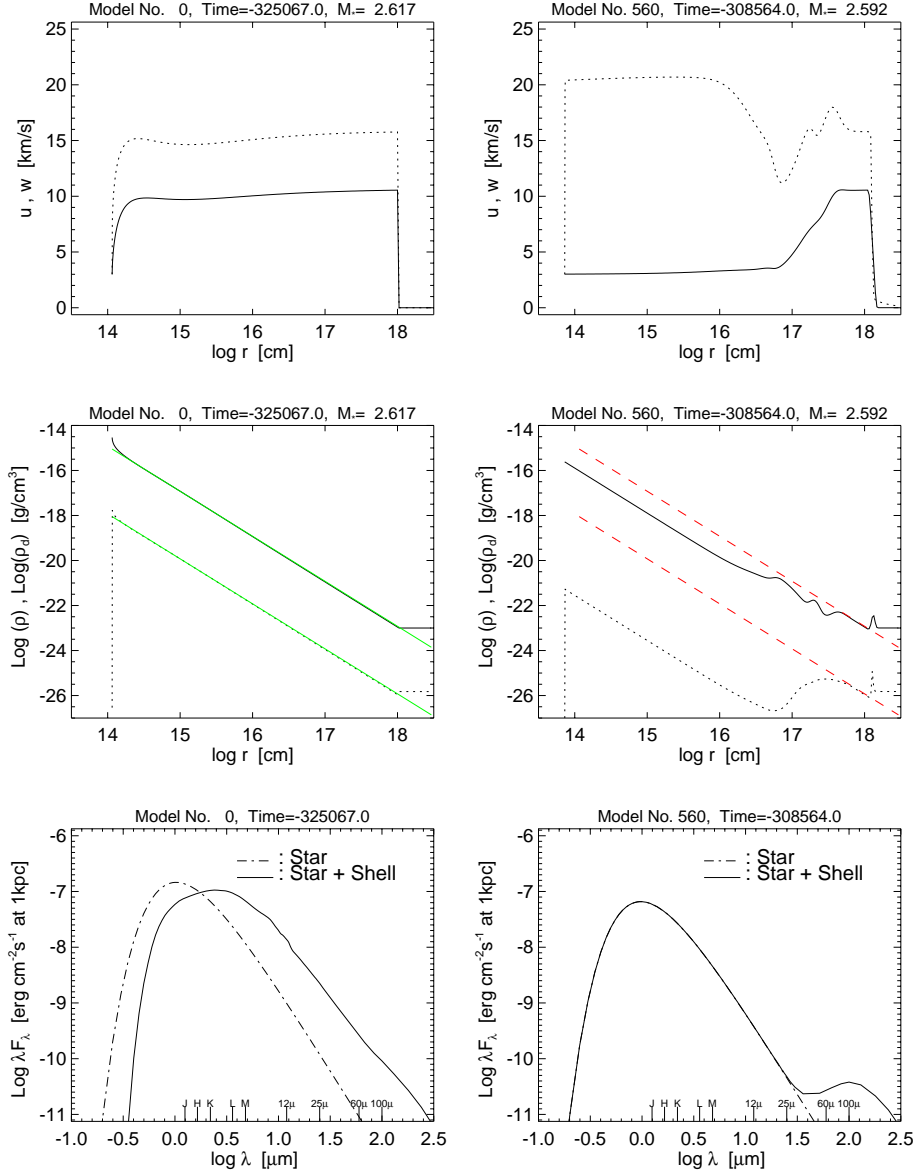


Fig. 3. Velocity field, density structure, and spectral energy distribution at two different times for the model sequence based on the stellar evolution data shown in Fig. 2. Dust is assumed to consist of grains of *amorphous carbon*. The left hand panels show the *initial conditions* for the time dependent calculations, corresponding to a steady state solution for stellar parameters and mass loss rate at time $t = -325\,067$ yr (time “A” in Fig. 2), modified in the outer regions such that $\rho \equiv 10^{-23}$ g/cm³ and the outflow velocity is zero to represent the presence of the interstellar medium. The right hand panels are for time $t = -308\,564$ yr, roughly corresponding to the time of minimum mass loss rate between “B” and “C” (see Fig. 2). **Upper panels:** gas (solid) and dust velocity (dotted) as a function of radial distance. **Middle panels:** radial distribution of gas (solid) and dust density (dotted). In both panels, the two faint dashed lines indicate the r^{-2} (gas-/dust) density laws representing the initial steady state solution. **Lower panels:** stellar input spectrum (dot-dashed) and the emergent spectral energy distribution (solid) which is the result of processing of the stellar radiation by the dusty envelope. Time and current stellar mass are given in the frame headers.

of amorphous carbon with properties as given in Table 1. The initial velocity at the dust formation point r_1 is assumed to be constant ($u_1 = 3$ km/s) throughout the sequence.

4.1.1. From the initial model through the ‘first’ thermal pulse

The initial model was obtained as a steady state solution (see Paper I) for stellar parameters and mass loss rate at time $t = -325\,067$ yr (corresponding to time “A” indicated in Fig. 2). Subsequently, the steady state solution was modified in the outer regions such that $\rho \equiv 10^{-23}$ g/cm³ and the outflow velocity is zero to represent the presence of the interstellar medium (cf. Sect. 2.3). Obviously, it is unrealistic to introduce the interstellar medium in this way since it will have been pushed much farther out by the stellar outflow during the previous evolution. The only reason for doing so is to demonstrate that the interaction of the slow AGB wind with the ISM is not producing any major observable features in the stellar spectrum; in particular, it will

be seen that it has nothing to do with the formation of detached shells.

Velocity field, density structure, and spectral energy distribution of the model serving as the initial condition for the time dependent calculations are shown in the left-hand panels of Fig. 3. The properties of steady state models have been described in detail in Paper I. We notice that typically such models show a constant gas outflow velocity of the order of 10 km/s over a wide radial range, leading to a radial density dependence $\rho \sim r^{-2}$. The ratio of dust and gas density is approximately constant and corresponds to the assumed dust-to-gas ratio of $\delta=0.0015$, multiplied by the factor u/w ($f_{\text{cond}}=1$ since $\dot{M} > 3 \cdot 10^{-7} M_{\odot} \text{ yr}^{-1}$, see Eqs. 19 and 20).

After about 18 000 yrs, the stellar luminosity and mass loss rate have dropped to a local minimum and conditions have changed significantly. The right hand panels of Fig. 3 show the situation at time $t = -308\,564$ yr, roughly corresponding to the time of minimum mass loss rate between “B” and

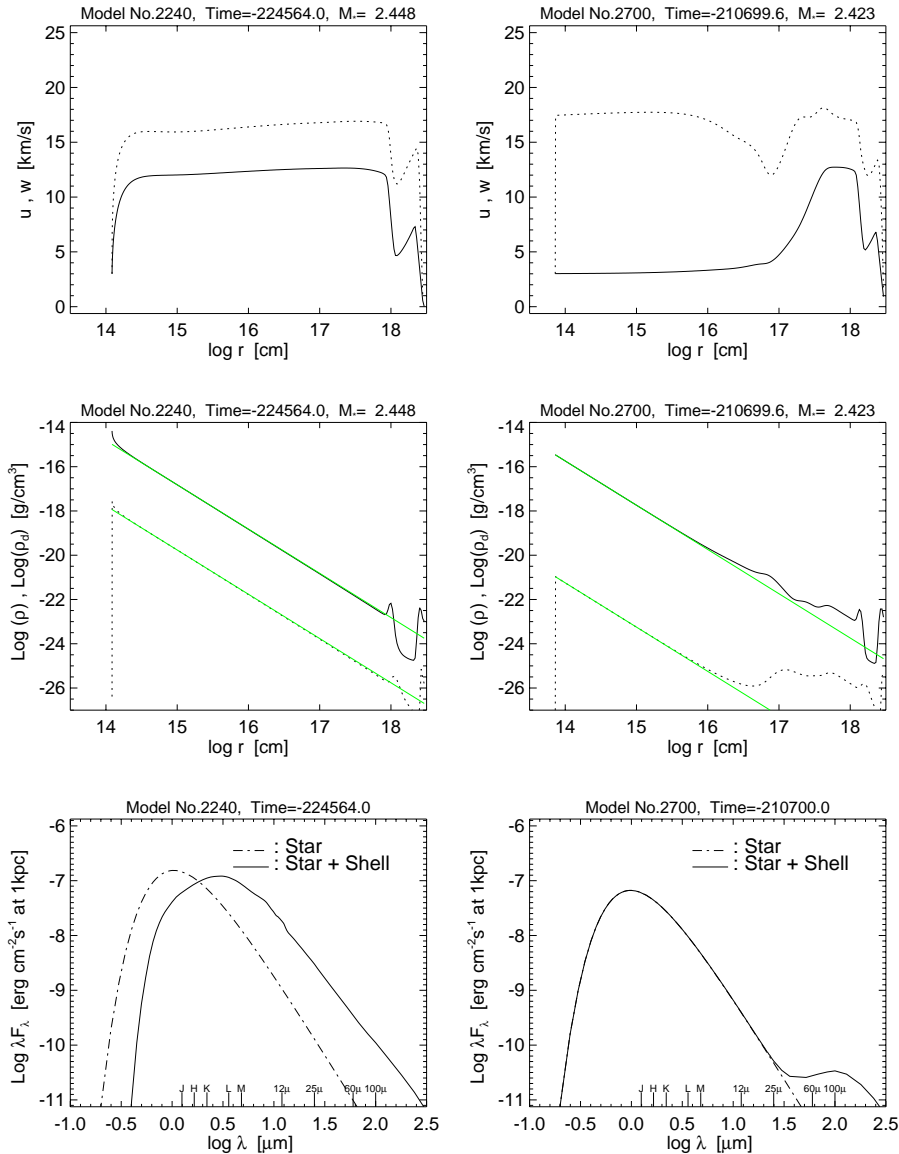


Fig. 4. Same as Fig. 3 but for times $t = -224\,564$ yr (left hand panels), roughly corresponding to time “D” indicated in Fig. 2 and $t = -210\,700$ yr (right hand panels), roughly corresponding to the time of minimum mass loss rate between “D” and “E” in Fig. 2. Notice that, in this and the following figures of this type, the r^{-2} reference lines in the density plots are scaled to match the actual density profiles at $r = 1\,10^{15}$ cm, unlike in Fig. 3 where they represent the initial steady state.

“C” (see Fig. 2). Due to the low mass loss rate the *gas* density in the inner part of the shell has decreased by almost two orders of magnitude. In addition, f_{cond} is now only 0.01 since $\dot{M} < 10^{-7} M_{\odot} \text{ yr}^{-1}$, as may be seen from Fig. 2. As a result, the *dust* density has dropped by almost four orders of magnitude (see middle panels) and the frictional coupling between gas and dust is no longer sufficient to drive the outflow, as indicated by the low gas outflow velocity, $u \approx 3$ km/s, and the high velocity of the dust component, $w \approx 22$ km/s. Rather the gas is driven solely by virtue of the “shock waves”, g_{shock} (see Eq. 2).

However, in the outer part of the shell ($r > 3\,10^{17}$ cm), velocity and density still more or less correspond to the much higher mass loss rate before the onset of the thermal pulse. This means that a *detached shell* has been created which, in the present case, is much more pronounced for the dust component than for the gas component. The main reason for the different behavior of the dust and gas components is the \dot{M} -dependent factor f_{cond} and the fact that the dust velocity in the

inner parts has increased by a factor of ≈ 2 while the gas velocity has decreased by a factor of ≈ 3 . In the emergent spectrum, the detached dust shell is clearly seen as a conspicuous excess emission beyond $\lambda \approx 25\,\mu\text{m}$ (lower panels).

Finally, we notice that at the boundary between the stellar wind and the “interstellar medium” some matter has been piled up, giving rise to a local density enhancement near $1.5\,10^{18}$ cm. At the same time, this interaction front has been pushed outward somewhat, while in the outermost parts of the model the interstellar medium is still unaffected (note that $g_{\text{shock}} \equiv 0$ in the outer parts of the model). In the considered wavelength range of the emergent spectrum we do not see any signature indicating the interaction of the stellar wind with the ISM.

4.1.2. Further evolution

During the further evolution the mass loss rate increases steadily for about 80 000 years and replenishes the inner low-density

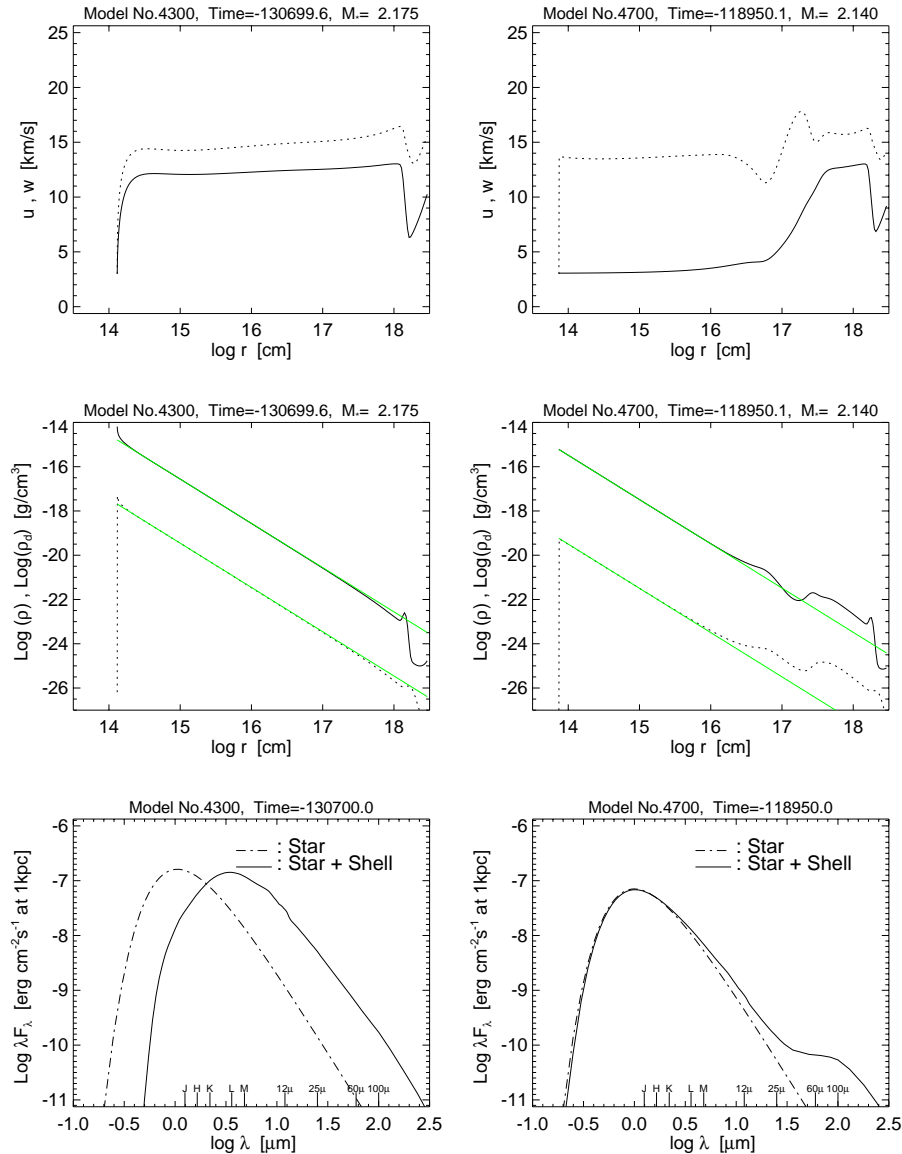


Fig. 5. Same as Fig. 3 but for times $t = -130\,700$ yr (left hand panels), roughly corresponding to time “F” indicated in Fig. 2 and $t = -118\,950$ yr (right hand panels), roughly corresponding to the time of minimum mass loss rate between “F” and “G” in Fig. 2.

regions of the shell. After some time the dust condensation becomes efficient again ($f_{\text{cond}}=1$) and the number density of dust grains exceeds the critical limit for driving the outflow. The left-hand panels of Fig. 4 show the situation at time $t = -224\,564$ yr (time “D” in Figs. 2 and 10), just before the onset of the next thermal pulse. The velocity and density structure closely resemble that of the initial steady state model, except in the outermost regions that still exhibit the signature of the previous thermal pulse. The pronounced density minimum near $r = 2 \cdot 10^{18}$ cm is the result of the extended mass loss rate minimum between “B” and “C”. The emergent SED is not sensitive to the conditions in the outermost parts of the shell and hence is very similar to that of the initial steady state solution, again showing a monotonic decrease of the flux towards longer wavelengths. Since luminosity and mass loss rate are somewhat higher than initially, the gas outflow velocity is somewhat higher while the drift velocity $w - u$ has slightly decreased. Due to the slightly increased overall density, the emergent spectral energy distribution has

shifted slightly to the red. Notice that the “interstellar medium” has meanwhile almost been pushed out of the computational domain. Its presence is only indicated by the low velocities near the outer boundary.

At the next minimum of the mass loss rate at time $t = -210\,700$ yr (right-hand panels of Fig. 4), the coupling between gas and dust has again become insufficient to drive the outflow due to the low dust density, as indicated by the slow (3 km/s) gas flow which is supported only by the assumed “shock wave pressure”. In the outer regions the gas velocity still is about 11 km/s, corresponding to the outflow velocity before the mass loss rate began to decrease. In the inner regions, the dust density is again very low and follows a $\rho_d \sim r^{-2}$ law out to $r \approx 10^{16}$ cm. Farther out, however, we see a distinct increase of the dust density with a local maximum near $r \approx 3 \cdot 10^{17}$ cm, representing again a *detached dust shell*. In the emergent spectrum, this excess concentration of dust is seen as an unmistakable excess emission at $\lambda > 25 \mu\text{m}$.

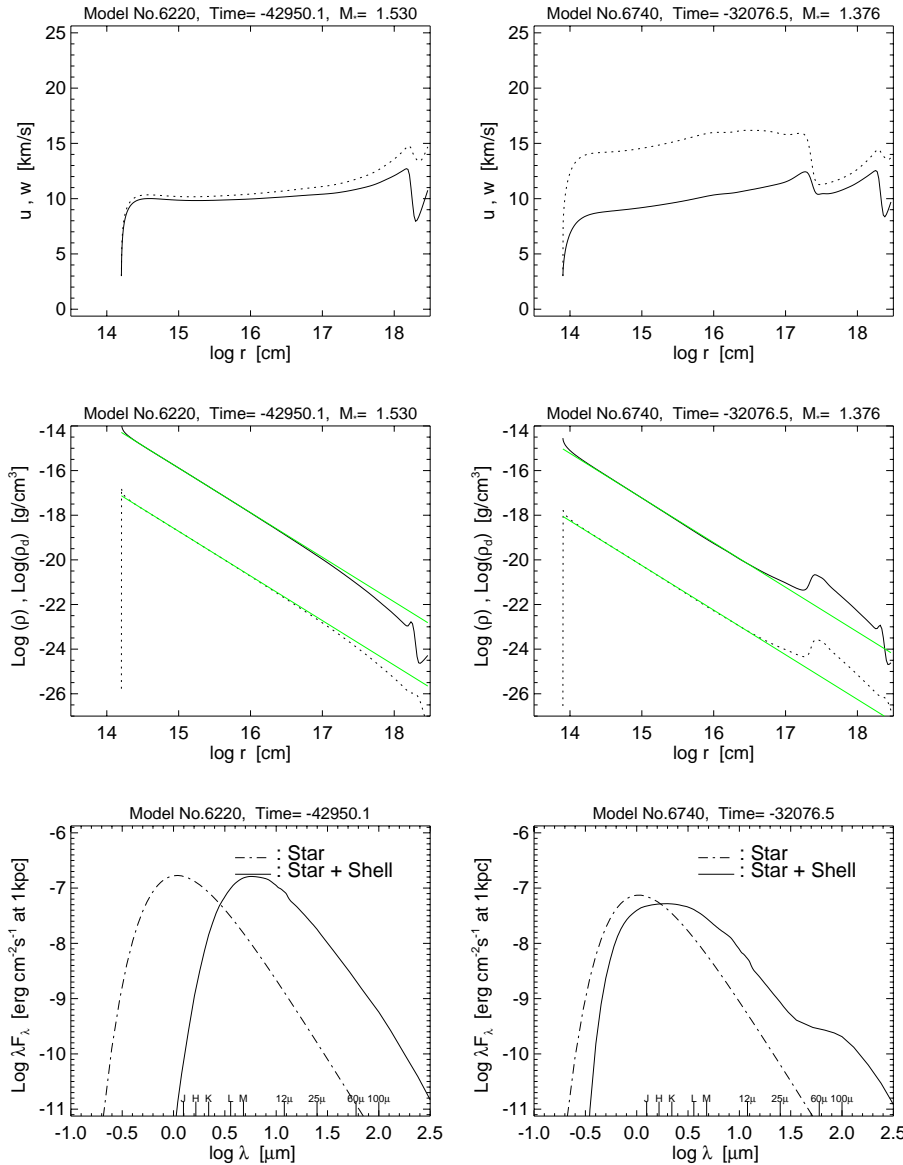


Fig. 6. Same as Fig. 3 but for times $t = -42\,950$ yr (left hand panels), roughly corresponding to time “H” indicated in Fig. 2 and $t = -32\,077$ yr (right hand panels), roughly corresponding to the time of minimum mass loss rate between “H” and “I” in Fig. 2.

The general hydrodynamical structure at this time is very similar to that during the mass loss minimum of the ‘first’ thermal pulse. Note, however, that the detached dust shell is somewhat broader due to the fact that duration of the period of reduced dust condensation efficiency ($f_{\text{cond}} < 1$) is significantly shorter for the ‘second’ thermal pulse, as may be seen by following the dotted horizontal lines in Fig. 2.

The same sequence of events occurs when we follow the evolution from the ‘second’ to the ‘third’ thermal pulse. The general hydrodynamical structure and emergent energy distribution before the onset of the ‘third’ thermal pulse, shown in the left-hand panels of Fig. 5, is again very similar to the situation encountered before the previous thermal pulse. Due to the higher mass loss rate the overall density is somewhat larger, the drift velocity is somewhat reduced, and more of the stellar radiation at visible wavelengths is absorbed by the circumstellar dust and reradiated in the infrared. The interstellar medium has now been completely pushed out of the computational domain.

During the following minimum (right-hand panels of Fig. 5), the mass loss rate no longer falls below $\dot{M} = 10^{-7} M_{\odot} \text{yr}^{-1}$. Hence, the dust condensation efficiency is hardly reduced ($f_{\text{cond}} \approx 0.5$). Nevertheless, we see that the dust density is still insufficient to couple efficiently to the gas component and to drive the outflow. The gas velocity is still only about 3 km/s in the inner shell, while it is about 12 km/s in the outer shell. As before, a detached shell has formed. However, it is apparent that the radial structure of the dust shell is now much more similar to that of the gas shell. This is because the temporal variation of the factor f_{cond} is now largely reduced and because the drift velocity in the outer parts is relatively small. Since the dust density in the detached shell is now significantly higher than during the previous thermal pulse, the absolute fluxes near 60 and 100 μm are now distinctly enhanced. At visual wavelengths, however, the shell is optically thin and the central star freely visible.

During the following 76 000 years of evolution the mass loss rate increases by a factor of 100. Shortly before the ‘fourth’

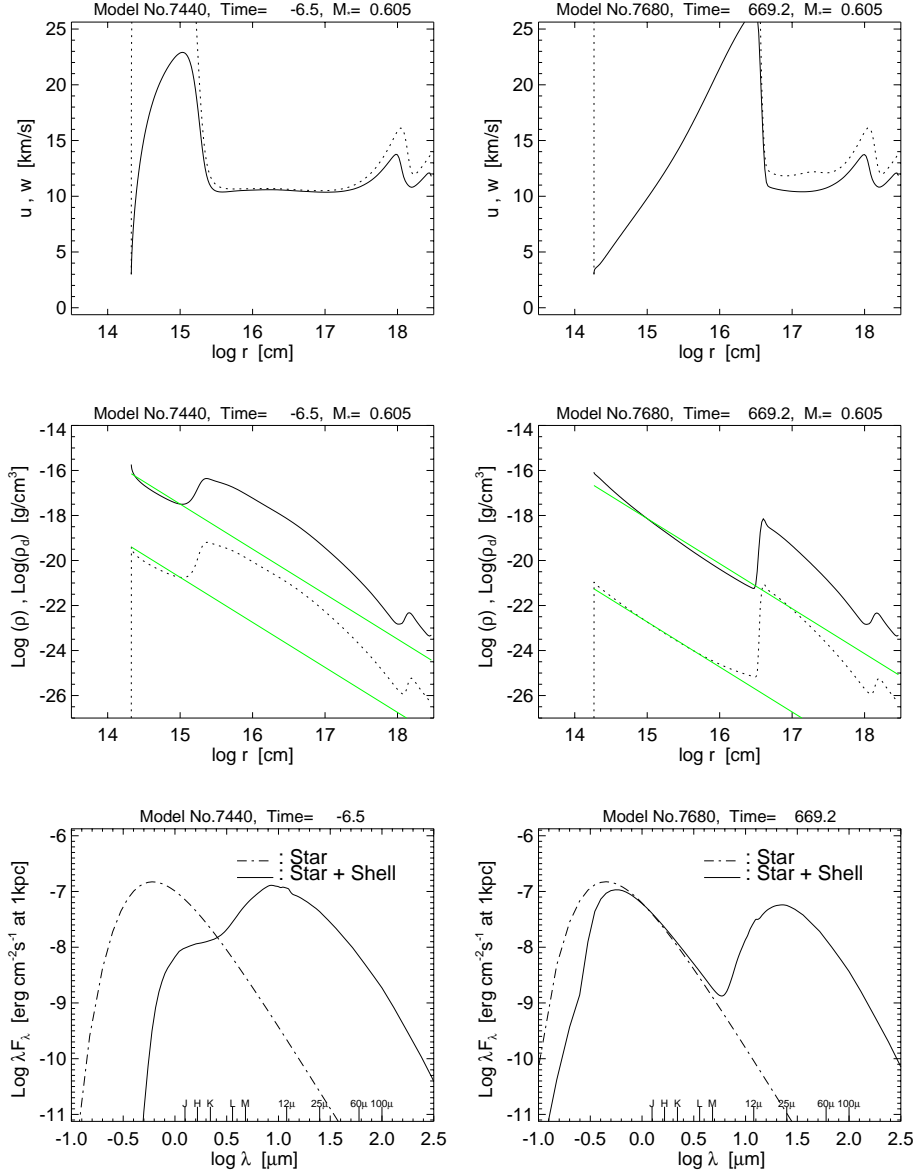


Fig. 7. Same as Fig. 3 but showing the situation at the end of the AGB evolution at times $t = -6.5$ yr (left hand panels; $T_{\text{eff}} = 6050$ K, maximum dust velocity $w = 50$ km/s), roughly corresponding to time “J” indicated in Fig. 2, and at $t = +669$ yrs into the post-AGB evolution (right hand panels; $T_{\text{eff}} = 8500$ K, maximum dust velocity $w = 120$ km/s).

and final thermal pulse occurs, the model AGB star has become completely obscured by the surrounding dust shell: the optical depth in the visual ($\lambda = 0.55 \mu\text{m}$) is $\tau_V \approx 33$. The plots for time $t = -42950$ yr (left-hand panels of Fig. 6) show that the outflow velocity is slightly lower than before the ‘third’ thermal pulse. The reason is that due to the larger optical depth (densities have increased by a factor of 10) fewer high-energy photons are now available to accelerate the dust grains. In the outer parts the density structure deviates markedly from the usual $\rho \sim r^{-2}$ law, reflecting the more pronounced (compared to the earlier cycles) temporal increase of the mass loss rate during the previous evolution.

At the minimum at time $t = -32077$ yr (right-hand panels of Fig. 6) the dust density is still sufficient to drive the outflow without the support of “shock waves”, although only marginally. As before, a detached shell has formed due to the steeply decreasing mass loss rate. For the reasons given above, the spatial structure of the gas and dust shell are now almost identical. At a

mass loss rate of $\dot{M} = 10^{-6} M_{\odot} \text{yr}^{-1}$ we find the visual optical depth to be $\tau_V \approx 2$, so the optical visibility of the central AGB star is still somewhat reduced. The hump in the spectral energy distribution near $\lambda 60$ and $100 \mu\text{m}$ clearly indicates the presence of a detached dust shell.

4.1.3. End of the AGB evolution

At the end of the AGB evolution, when mass loss rate is at its maximum ($\dot{M} \approx 1.3 \cdot 10^{-4} M_{\odot} \text{yr}^{-1}$, $L_* \approx 6500 L_{\odot}$ in our example), the visual optical depth of the dust shell is $\tau_V \approx 140$ and the outflow velocity in the inner shell is quite uniform, about 10 km/s. This is at the lower end of outflow velocities observed in dusty carbon stars (cf. Habing et al. 1994, Fig. 8), indicating that the luminosity of our stellar model and/or the adopted dust-to-gas ratio is somewhat low. Increasing L_* and δ by a factor of 2 would lead to a more typical outflow velocity close to 20 km/s according to the scaling relations given by Habing et al. (1994).

After the mass loss rate has dropped to the Reimers rate ($\dot{M} \approx 3 \cdot 10^{-7} M_{\odot} \text{ yr}^{-1}$) at time $t = 0$ (left-hand panels of Fig. 7), density in the innermost shell has diminished by almost three orders of magnitude and the central star begins to shine through the expanding shell again ($\tau_V \approx 8$). Since the dust in the inner regions is now exposed to the unobscured stellar radiation, which moreover now originates from a star with greatly reduced mass and rapidly increasing effective temperature, it is strongly accelerated and reaches a maximum velocity of $w \approx 50$ km/s. Despite the low coupling, the gas component is initially also strongly accelerated up to more than 20 km/s. The radial density distribution clearly reflects the steadily increasing mass loss rate before the end of the AGB evolution in the outer parts of the shell and the subsequent sharp drop from the AGB to the Reimers mass loss rate in the inner parts, resulting in a characteristic shape distinctly different from the simple $\rho \sim r^{-2}$ relation.

We extended our hydrodynamical simulations somewhat into the post-AGB regime, using the mass loss prescription shown in the upper panel of Fig. 19. After 660 yrs of post-AGB evolution (see right-hand panels of Fig. 7) the gas/dust shell has completely detached from the star which has increased its effective temperature to $T_{\text{eff}} \approx 8500$ K. Due to the low Reimers mass loss rate the gas density in the inner part of the shell is very low, and the dust moves outward with high speed ($w > 100$ km/s) since it is largely decoupled from the gas. As a result, the inner shell is now essentially devoid of hot dust, even though still $f_{\text{cond}} = 1$: the visual optical depth is $\tau_V \approx 0.5$, and the central star is again unobscured at optical wavelengths. The dust density distribution during this phase of evolution produces a characteristic double-peaked spectral energy distribution shown in the lower right panel.

The transition from the AGB to the post-AGB phase is discussed in more detail in Sect. 5.4.

4.1.4. Summarizing the dynamical evolution of the shell

The sequence of events described in the previous sections demonstrates that the time-dependence (on stellar evolution time scales) of the density structure and velocity field of a circumstellar AGB shell is probably quite complex. In order to summarize the main features, we display in Fig. 8 the temporal evolution of the gas and dust velocity (top), the gas and dust density (middle) as well as the dust temperature (bottom) at an intermediate radial position, $r = 3 \cdot 10^{17}$ cm, over the time interval of $\approx 325\,000$ yrs covered by the simulation discussed above.

Obviously, the gas velocity prefers one of two distinct states: when the mass loss rate is below some critical limit, the coupling between gas and dust is insufficient to drive the outflow via radiation pressure on dust and the flow is essentially driven by the artificial acceleration term g_{shock} representing the pressure of the shock waves produced by the stellar pulsation. In this state, $u \approx 4$ km/s, and the drift velocity of the dust relative to the gas is largest during these periods. For sufficiently high mass loss rates, on the other hand, the driving mechanism based on the radiation pressure on dust is taking over and leads to

$u \approx 10$ km/s. At the same time the dust drift is relatively small due to the close coupling of dust and gas. Note that the duration of the periods of low outflow velocity decreases in the course of the AGB evolution, because on average \dot{M} increases with time and falls less deeply below the critical limit for each consecutive thermal pulse.

The temporal variation of the gas density closely follows the variations of the mass loss rate enforced at the inner boundary of the shell. However, it is modified by the time-dependence of the gas velocity, leading to a reduced amplitude of the overall gas density fluctuations (since u is small when \dot{M} is low and vice versa). One important point to note here is that while the extended periods of low mass loss rate are clearly seen in the $\rho(t)$ data at $r = 3 \cdot 10^{17}$ cm, the short-term variations of the mass loss rate (labeled ‘2’, ‘3’ in Fig. 10) occurring before the eventual long-term decline of \dot{M} are *not* detectable. Obviously, the associated density fluctuations are smeared out quickly by hydrodynamical effects and have largely disappeared before reaching the outer regions of the shell. We have checked that the small-scale density structure does *not* disappear due to numerical limitations (e.g. due to the deteriorating spatial resolution of the numerical grid with radial distance). It is a consequence of the rather complex physical behavior of the system, related to the fact that, due to optical depth effects, the outflow velocity is a non-monotonic function of the mass loss rate. As a consequence, the density peak related to mass loss “eruption” ‘3’ runs into the density depression related to the preceding short mass loss reduction ‘2’, resulting in a partial cancellation of the density fluctuations. The usual assumption that the outflow velocity is independent of mass loss rate, often made in semi-empirical models of time-dependent dusty outflows (recent examples: Groenewegen & de Jong 1994; Shu 1997; Shu & Jones 1997), is clearly not valid in this case (for details see Steffen & Schönberner 1998).

Surprisingly, however, we see strong short-term density enhancements (of a factor of 3 to 4) near the end of the phases of low mass loss rate (see middle panel near $t = -250\,000, -170\,000, -90\,000$ yrs). These are caused by local compression of the gas where matter with higher velocity runs into regions of lower velocity and higher density: the density peaks coincide with the times of steep velocity increase, i.e. they are related to the switch over from a slow, “shock-driven” to a faster, “dust-driven” wind. Note that the transition from the slow to the fast wind happens quite abruptly when the mass loss rate exceeds a critical limit ($\dot{M} \approx 10^{-6} M_{\odot} \text{ yr}^{-1}$). It has nothing to do with the assumed time-dependent dust condensation efficiency $f_{\text{cond}}(\dot{M})$, but is a general property of the dust-driven wind: below a critical wind density, the coupling between dust and gas is insufficient and the gas outflow cannot be maintained; for wind densities even slightly above this limit, however, the outflow is accelerated efficiently. This property inevitably leads to an almost bimodal dependence of the outflow velocity on the mass loss rate, and consequently to the formation of *wind interaction regions*. These manifest themselves as thin shells of enhanced gas density (and probably enhanced gas temperature as well). We propose that these features are related to the ori-

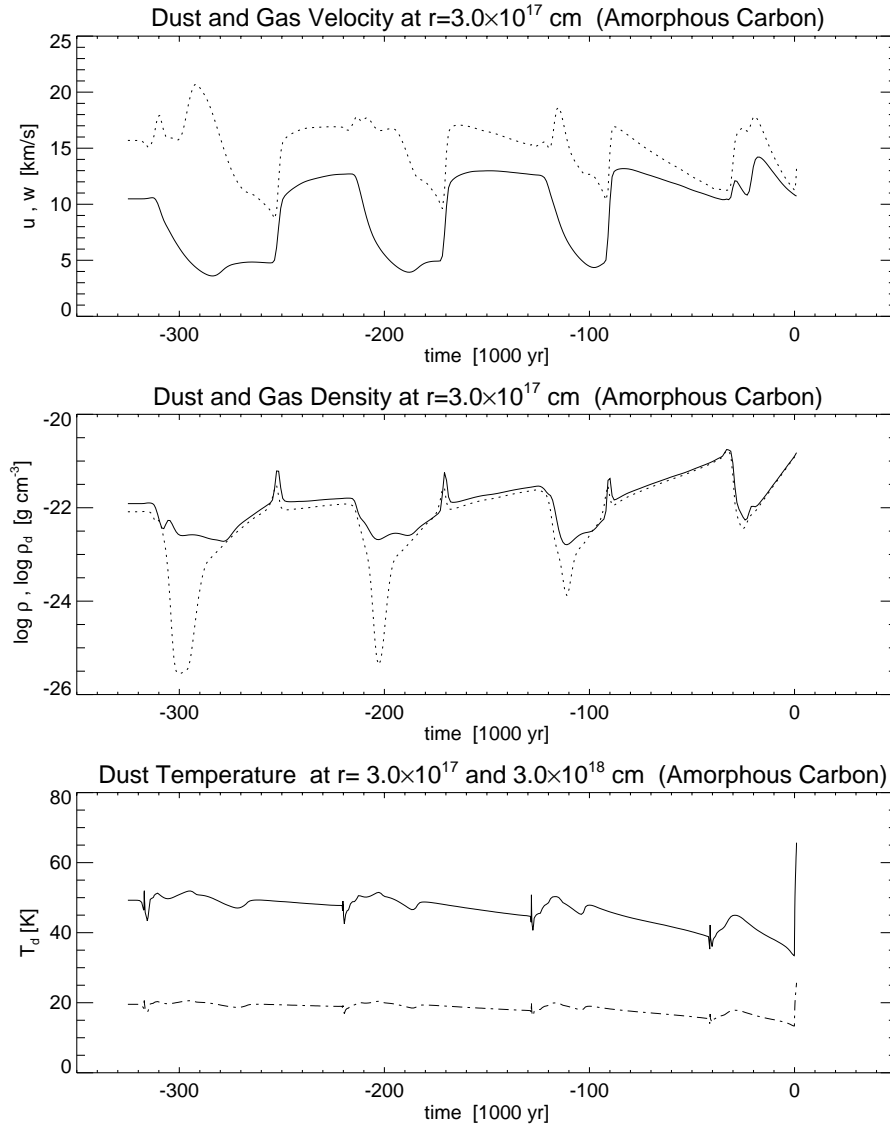


Fig. 8. Top: Gas velocity (solid) and dust velocity (dotted) as a function of time at a distance of $r = 3 \cdot 10^{17}$ cm from the star (data re-interpolated from the moving grid to constant r). Data are taken from the model sequence computed with amorphous carbon dust, for which details are shown in Figs. 3 to 7. **Middle:** Similar plot of the gas density (solid) and the dust density (dotted). For a more direct comparison, the dust density has been divided by the dust-to-gas ratio, $\delta = 0.0015$. **Bottom:** Temporal variation of the dust temperature at $r = 3 \cdot 10^{17}$ (upper) and $r = 3 \cdot 10^{18}$ cm (lower curve). The general time-dependence of the dust temperature, including the sharp final increase reflects the variation of the stellar luminosity and effective temperature, modified by the temporal variation of the optical depth.

gin of the very thin molecular shells detected in CO emission around a number of carbon stars by Olofsson et al. (1998). This point is further discussed in a separate publication (Steffen & Schönberner 1998).

The dust density closely follows the gas density, except for some phase shift caused by the fact that the dust velocity is, at times, significantly higher than the gas velocity. And, of course, the dust density is reduced by an additional factor of up to 100 whenever $\dot{M} < 3 \cdot 10^{-7} M_{\odot} \text{ yr}^{-1}$ (cf. Sect. 2.5), an effect more pronounced during the earlier thermal pulses.

The dust temperature T_d at $r = 3 \cdot 10^{17}$ cm varies between 55 and 35 K. At the outer boundary of our model ($r = 3 \cdot 10^{18}$ cm), T_d is close to 20 K. Remembering that T_d is computed as the radiative equilibrium temperature of the dust grains, it is evident that, at a fixed distance from the star, T_d depends on the stellar luminosity and effective temperature, as well as on the column density of dust between the central star and the considered radial position. In this sense the temporal variation of T_d seen in the lower panel of Fig. 8 can be understood as the

combined effect of the temporal variation of $L_*(t)$, $T_{\text{eff}}(t)$, and $\dot{M}(t)$ which determines the column density, i.e. optical depth, in a non-local way. One can clearly see that the dust temperature increases during the mass loss minima when the absorption of the stellar radiation by the intervening dust diminishes and the flux spectrum incident on the dust grains shifts to shorter wavelengths. The final sharp rise of T_d is caused by the greatly reduced optical depth of the inner dust shell, combined with a considerable increase of the stellar effective temperature at the beginning of the post-AGB phase.

Finally, we point out that all the time-dependent hydrodynamical features discussed above do *not* depend on the assumed time-dependence of the dust condensation efficiency factor f_{cond} (see Eqs. 19, 20). A test run with $f_{\text{cond}} \equiv 1$ shows very much the same temporal behavior as seen in Fig. 8.

4.2. Model calculations for a shell with silicate dust

The model sequence described above was based on the assumption that the dust condenses as grains of amorphous carbon (AC).

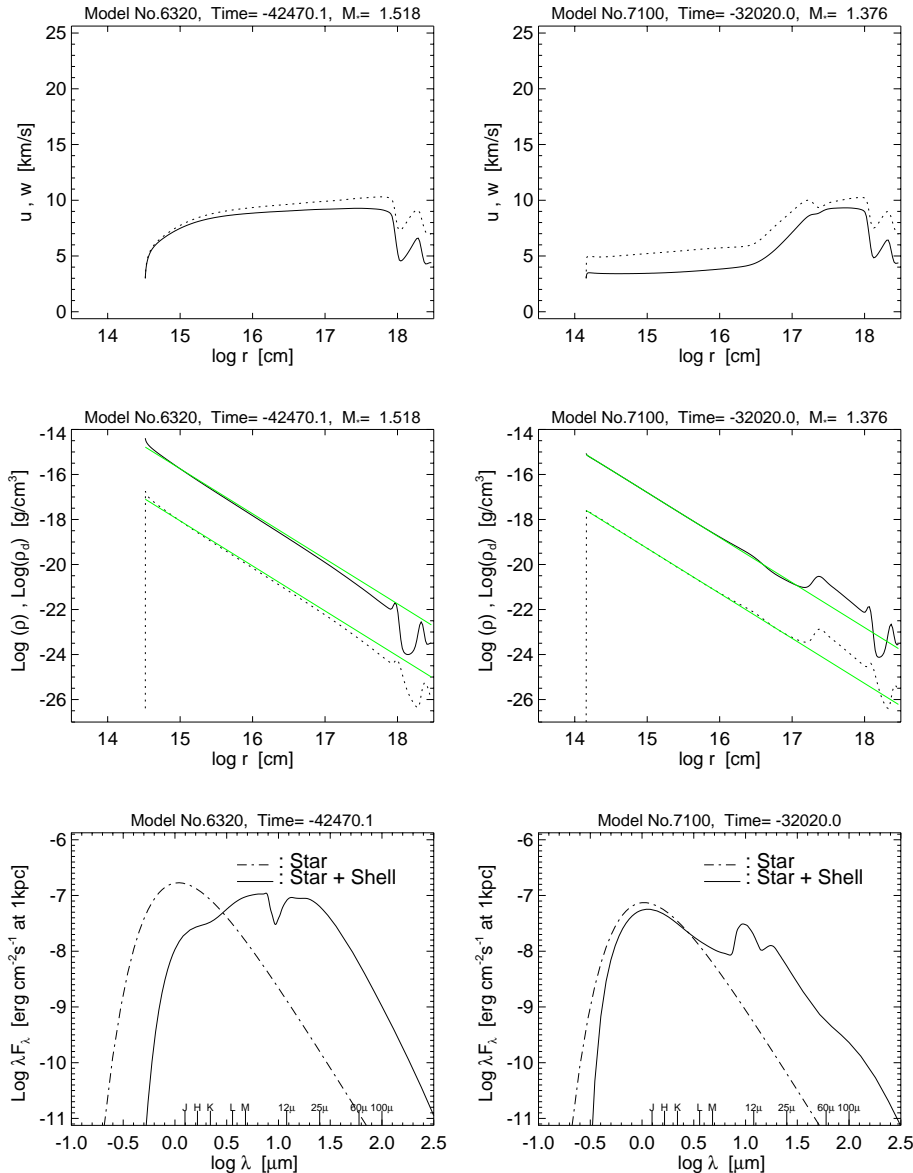


Fig. 9. Velocity field, density structure, and spectral energy distribution at two different times from the model sequence computed with dust grains composed of “astronomical” silicates. The times are $t = -42\,470$ yr (left hand panels), roughly corresponding to time “H” indicated in Fig. 2, and $t = -32\,020$ yr (right hand panels), roughly corresponding to the time of minimum mass loss rate between “H” and “I” in Fig. 2. Note that the silicate features are seen in absorption before the thermal pulse and change into emission during the subsequent period of low mass loss rate. For comparison with the carbon star sequence, see Fig. 6.

We have computed another sequence assuming the dust to condense as grains of “astronomical” silicates (AS) with properties given in Table 1 (see Sect. 2.2). In all other respects the two sequences are identical. In particular, they are based on the same stellar evolution sequence $L_*(t)$, $T_{\text{eff}}(t)$, $\dot{M}(t)$ and cover the same period of time.

We do not discuss here the very details of the hydrodynamical evolution of the circumstellar shell with silicate dust, since this case is in principle very similar to the one presented for amorphous carbon dust. As an example, we only show the hydrodynamical structure and emergent spectral energy distribution before and after the final thermal pulse (Fig. 9). This plot is made for the same instants of time as Fig. 6 in order to allow a direct comparison.

The main differences arise from the different absorption properties of “astronomical” silicates. Assuming a fixed grain size of $a = 0.05 \mu\text{m}$, their extinction cross section per unit mass

is at least a factor of 5 lower than for amorphous carbon grains over the wavelength range 0.2 to $7 \mu\text{m}$, which is centered on the maximum of the stellar spectral energy distribution. However, due to the presence of the “silicate features”, the absorption cross section of AS exhibits strong local maxima near $\lambda 10$ and $20 \mu\text{m}$, where the extinction cross section per unit mass exceeds that of AC by up to a factor of 5. In comparison to the case of AC, this non-monotonic wavelength-dependence of the extinction efficiency of AS gives rise to a qualitatively different response to changes of the spectral energy distribution of the incident radiation.

The main difference, however, is the lower overall extinction efficiency of AS between 0.2 to $7 \mu\text{m}$. This leads to a lower average acceleration and outflow velocity (especially during the earlier thermal pulses), even though we adopted a higher dust-to-gas ratio for AS ($\delta = 0.005$, instead of $\delta = 0.0015$ for AC). As a consequence, the features in the density structure are

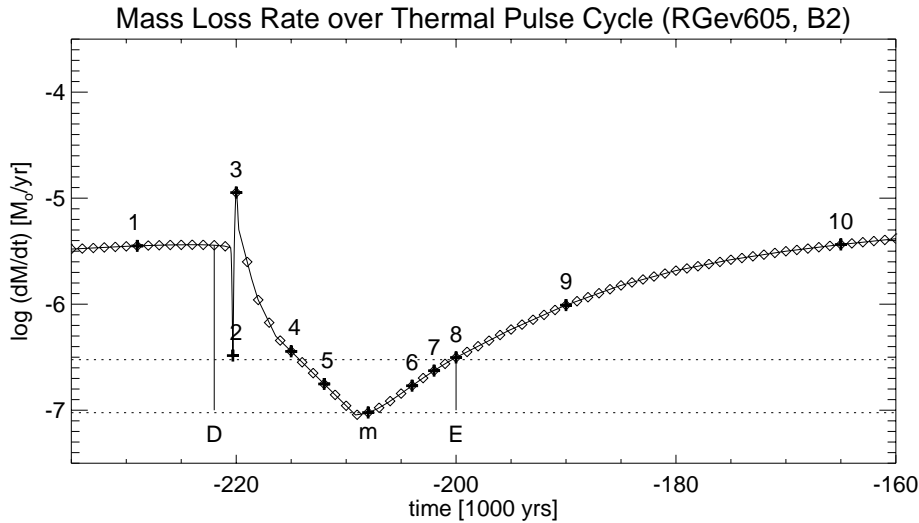


Fig. 10. Close-up of Fig. 2, showing the temporal variation of the mass loss rate of our standard stellar model ($M_i = 3 M_\odot$) during the ‘second’ thermal pulse cycle, about 200 000 yrs before the end of the AGB evolution. For mass loss rates higher than $3 \cdot 10^{-7} M_\odot \text{ yr}^{-1}$ (upper dotted horizontal line) the dust condensation fraction is assumed to be 100% of the value given in the last row of Table 1, dropping smoothly to 1% of this value for mass loss rates below $1 \cdot 10^{-7} M_\odot \text{ yr}^{-1}$ (lower dotted horizontal line). The times labeled “1” to “10” (and “m”) serve as reference points for the data shown in the following figures. The separation between two adjacent diamonds corresponds to 1000 yrs.

closer to the star at a given time (compare Figs. 6 and 9). Also, the average density of the outflow is somewhat higher, and the phase shift between the fluctuations of gas and dust density are more pronounced. Due to the higher overall dust density, there is hardly any excess emission at $\lambda 60$ and $100 \mu\text{m}$ in the example shown in Fig. 9.

In the following sections we will present a detailed comparison of the photometric properties derived from the sequences computed with amorphous carbon dust and with “astronomical” silicate dust, respectively.

4.3. Variation of emergent spectrum and surface brightness distribution during a thermal pulse cycle

In order to illustrate in more detail how the emergent spectral energy distribution changes during a typical thermal pulse cycle, we have chosen the pulse centered on $t \approx -210$ 000 yrs as an example. The time-dependence of the mass loss rate during this thermal pulse is fully resolved in Fig. 10.

4.3.1. Model fluxes for carbon stars

For the “carbon star” model sequence computed with amorphous carbon dust, which has been described in detail in the previous sections, we have evaluated the emergent spectral energy distribution and the spatial distribution of the surface brightness as a function of time.

As this model runs through the ‘second’ thermal pulse cycle, the emergent spectral energy distribution changes with time as illustrated in the upper panels of Fig. 11. At time t_1 the SED corresponds to that of a steady state model with $T_{\text{eff}} = 3500$ K, $L_* = 6500 L_\odot$ and $\dot{M} = 3 \cdot 10^{-6} M_\odot \text{ yr}^{-1}$. About 15 000 years later (time t_5), the SED has shifted considerably toward shorter wavelengths. Beyond $\lambda 25 \mu\text{m}$, however, the flux diminishes at a slower rate, leading to the development of a relative excess of emission in the IRAS pass bands centered on 60 and $100 \mu\text{m}$. As was demonstrated above (Sects. 4.1.1, 4.1.2), this is characteristic of the presence of a detached dust shell. As mass loss

resumes and replenishes the inner shell with hot dust, the spectral energy distribution gradually reddens and the flux maximum near $100 \mu\text{m}$ disappears. At time t_{10} , about 64 000 years after time t_1 , the mass loss rate has reached its former value and the spectra at times t_{10} and t_1 are practically indistinguishable.

This temporal variation of the emergent spectral energy distribution translates into an extended loop in leftmost part of the IRAS two-color-diagram, as shown in the lower panel of Fig. 11. Note that around the time of minimum mass loss rate the object spends several thousand years in region “VIa”, at positions in the IRAS two-color-diagram which are quite remote from the main color-color relation valid for steady state models for amorphous carbon dust (cf. Fig. 14 of Paper I). In contrast, the excursion into region “VIb” (t_2) takes less than 1000 yrs.

The time evolution of the radial distribution of the surface brightness at $\lambda 100 \mu\text{m}$, i.e. the emergent intensity projected onto the plane of the sky, is shown in the top panel of Fig. 13. At time t_m , in the middle of the extended period of mass loss “interruption”, the intensity distribution shows a local maximum at a distance of about $2 \cdot 10^{17}$ cm from the central star, corresponding to a ring-like structure on a surface brightness map. During the further evolution the position of maximum brightness moves outward. However, since this ring-like feature is rather broad (width ≈ 10 times separation from the star, see also middle right panel of Fig. 4) and the intensity contrast is very low, it will be hard to detect, unlike the associated excess emission in the SED, which is a prominent feature.

4.3.2. Model fluxes for oxygen stars

For the “oxygen star” model sequence computed with dust consisting of “astronomical silicates” (see Sect. 4.2), we have evaluated the emergent spectral energy distribution and the spatial distribution of the surface brightness in exactly the same manner as for the “carbon star” sequence.

The temporal variation of the emergent spectral energy distribution over the ‘second’ thermal pulse cycle is presented in the upper panels of Fig. 12. At time t_1 the SED corresponds to

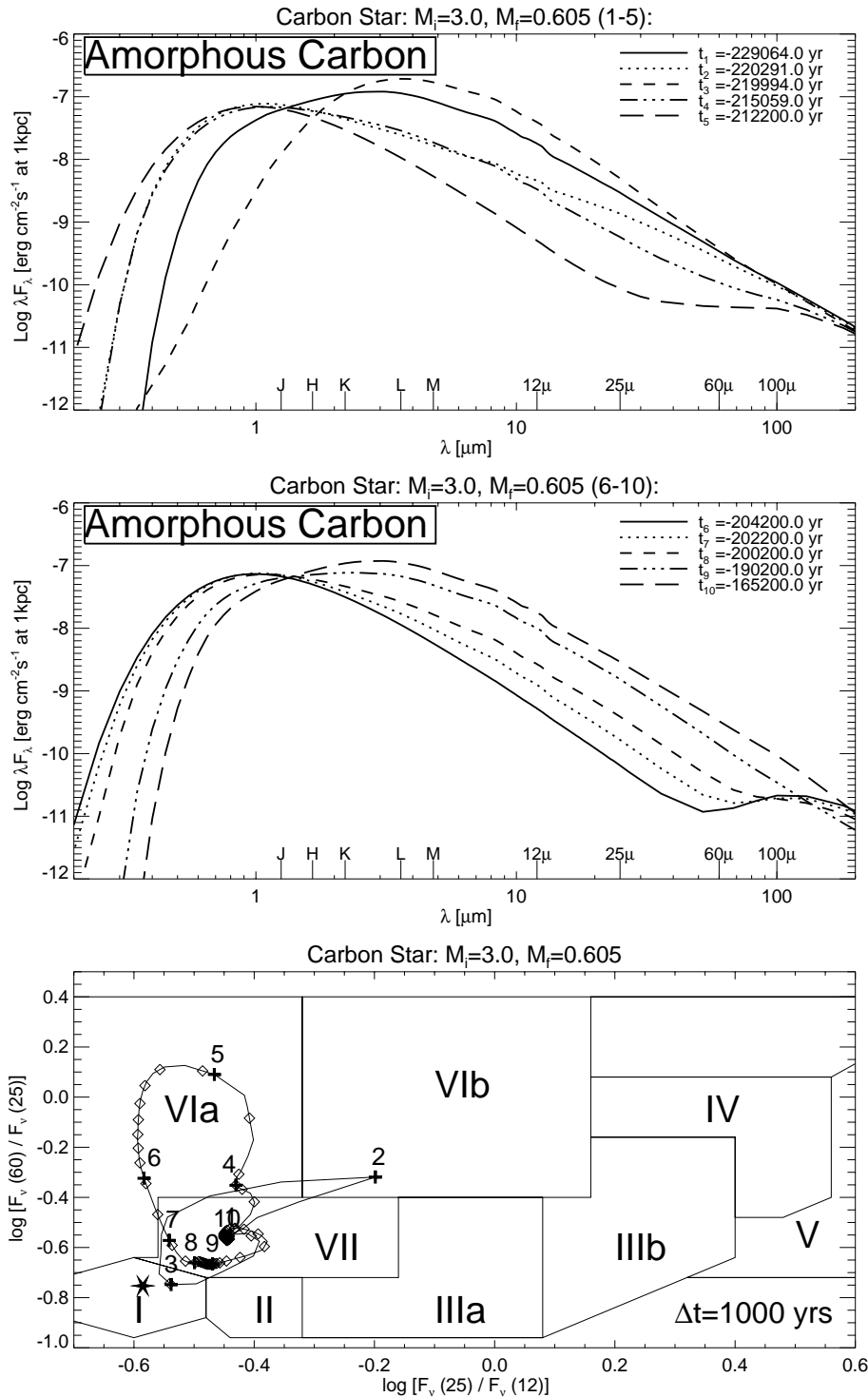


Fig. 11. Time sequence of spectral energy distributions over the thermal pulse cycle shown in Fig. 10, assuming the dust grains to be composed of *amorphous carbon* with properties as given in Table 1. The emergent spectra for times t_1 to t_5 (see labels in Fig. 10) are presented in the **upper panel**, while those for times t_6 to t_{10} are displayed in the **middle panel**. Note the pronounced excess emission at λ 60 and 100 μm at times t_5 and t_6 . The **lower panel** shows the corresponding loop of this object in the IRAS two-color-diagram, with positions at reference times t_1 to t_{10} indicated by + signs (the positions for t_1 and t_{10} coincide). Open diamonds outline the time evolution in steps of $\Delta t = 1000$ yrs. Note that the excursion to region “VIb” (t_2) is of very short duration. The “star” in region I marks the position of a black body with $T = 3000$ K. Subdivision into regions after van der Veen & Habing (1988).

that of a steady state model with $\dot{M} = 3 \cdot 10^{-6} M_\odot \text{yr}^{-1}$. The silicate features near λ 10 and 20 μm are seen in emission (with some self-absorption in the center of the 10 μm feature). At time t_4 the silicate features are still prominent. But only 3000 yrs later (t_5) they have essentially disappeared, since the inner parts of the shell are now almost devoid of “hot” dust. At the same time the “cool” dust, now located in a detached shell, stands out as an excess emission in the IRAS 60 and 100 μm pass bands. As

mass loss resumes and replenishes the inner shell with hot dust, the spectral energy distribution gradually reddens, the silicate emission features reappear and the signature of the detached dust shell in the far infrared vanishes. As in the case of the carbon star model, the spectra at times t_{10} and t_1 are practically indistinguishable.

The corresponding loop in the IRAS two-color-diagram is shown in the lower panel of Fig. 12. Note that this loop is more

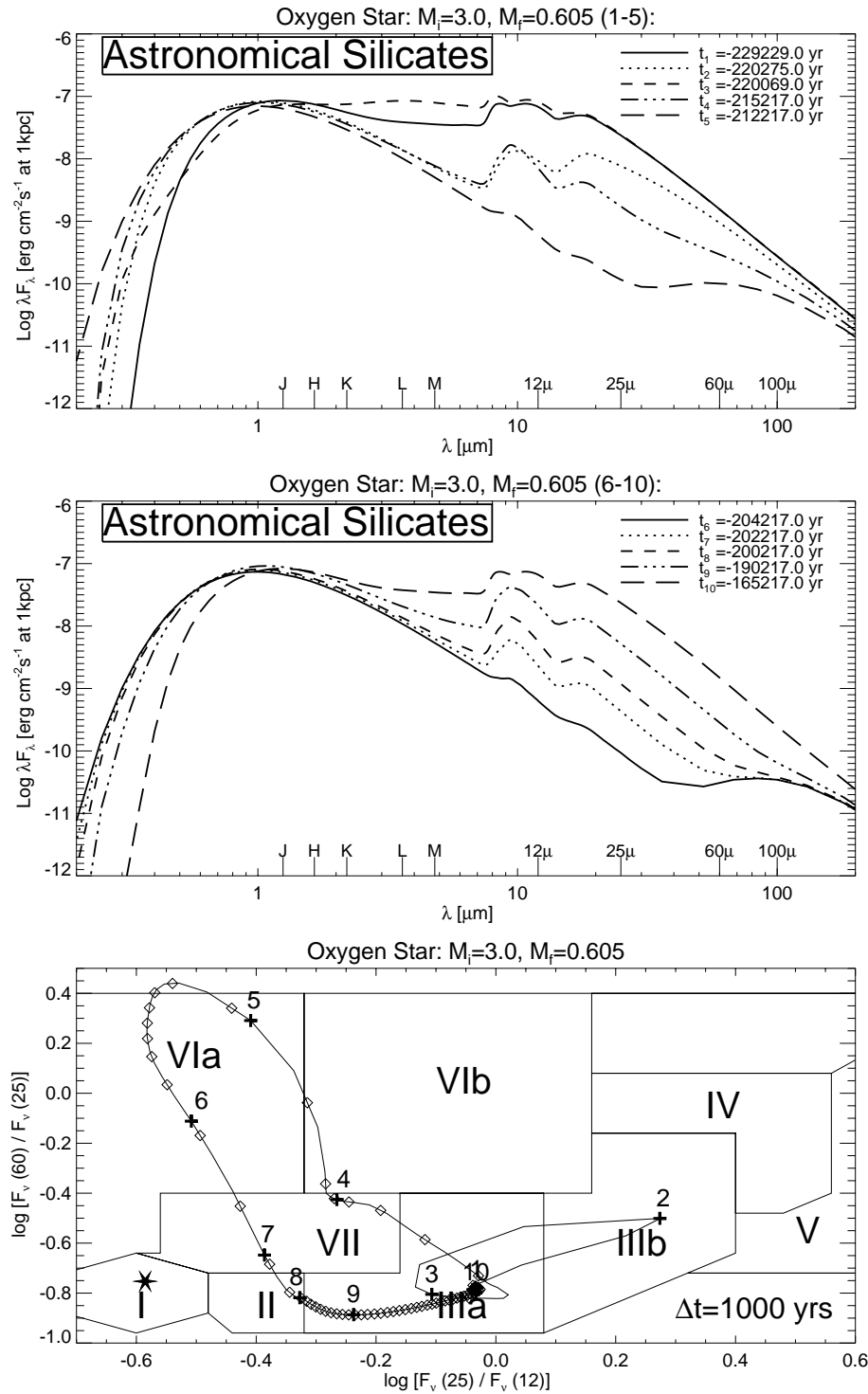


Fig. 12. Time sequence of spectral energy distributions (top and middle) and corresponding loop in the the IRAS two-color-diagram (bottom) over thermal pulse cycle shown in Fig. 10, based on the same stellar evolution sequence and presented in the same way as the results shown in Fig. 11, but now assuming the dust to be composed of “astronomical” silicates. Again, the colors at times t_1 and t_{10} are almost identical. Excess emission at λ 60 and $100 \mu\text{m}$ is again clearly seen at times t_5 and t_6 , while at the same time the silicate features at 9.7 and $18 \mu\text{m}$ are essentially absent. In contrast to the very short excursion to region “IIIb” (t_2), the extended loop into region “VIa” takes more than 10 000 years.

extended, both in horizontal and vertical direction, than the loop traced out by the carbon star model. The main reason is the different wavelength dependence of the silicate opacity: the starting point (time t_1) is located in a lower position in the IRAS two-color-diagram because the opacity gradient in the far infrared is steeper for “astronomical” silicates ($Q_{\text{abs}}(\text{AS}) \sim \lambda^{-2}$ while $Q_{\text{abs}}(\text{AC}) \sim \lambda^{-1}$); the loop starts farther to the right because due to the presence of the silicate emission features the

fluxes at 12 and $25 \mu\text{m}$ are initially almost equal. Since the silicate features temporarily disappear in the course of the thermal pulse, the ratio of the fluxes at 12 and $25 \mu\text{m}$ varies over a larger range than in the case of amorphous carbon dust. Consequently, the loop is more extended in the horizontal direction. The reason for the larger extent in the vertical direction is not so obvious. A comparison of the dust density distributions in the oxygen and carbon star outflows, respectively, reveals that due to the lower

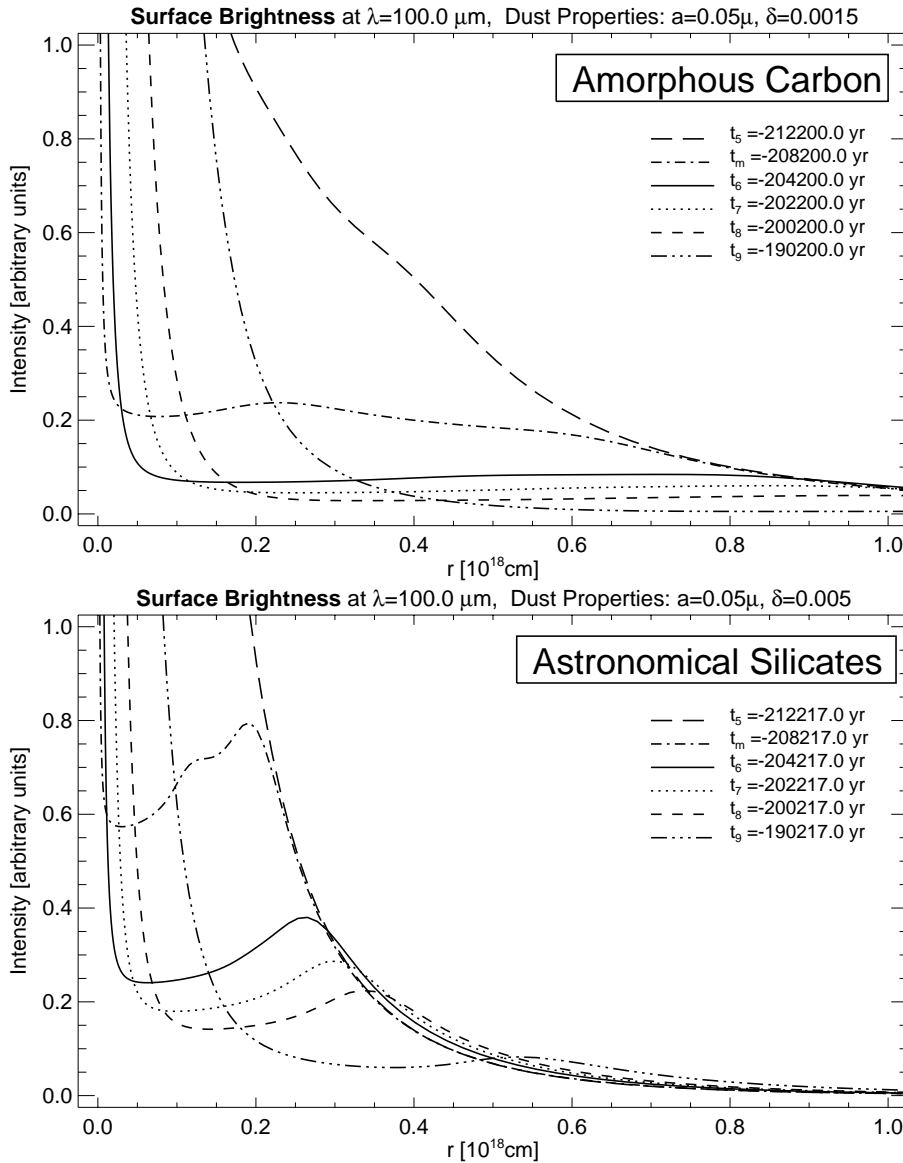


Fig. 13. Time evolution of the radial intensity distribution at $\lambda 100 \mu\text{m}$ showing the formation and development of a detached dust shell for part of the carbon star sequence (top) and part of the oxygen star sequence (bottom). Times t_5 to t_9 are identical to those used in Figs. 11 and 12, respectively. In addition, the intensity distribution has also been evaluated at time t_m , the time of the local minimum of the mass loss rate at $t \approx -209\,000$ yrs before the end of the AGB evolution (see also Fig. 10). Although intensity is given in arbitrary units, the scale is constant for each panel, so the relative variation of the intensity distribution within the two time sequences is reproduced correctly. Because of the higher dust velocity in the carbon star model (top), the dust shell is much more extended and located at greater radial distances than for the oxygen star model (bottom). In consequence, a detached dust shell is much more clearly visible in surface brightness maps produced for the oxygen star model than for the carbon star model, although in both cases the amount of excess emission at 60 and $100 \mu\text{m}$ is very similar (cf. Figs. 11 and 12, time t_6).

outflow velocities the density gradients are somewhat steeper in the former case. This leads to a larger amplitude of the color variations for the oxygen star model.

Note again that in the middle of the time interval of low mass loss rate, the loop of our oxygen star covers several different regions of the IRAS two-color-diagram, spending thousands of years at positions which are quite distinct from the main color-color relation valid for steady state models with silicate dust (cf. Fig. 12 of Paper I).

The time evolution of the surface brightness distribution at $\lambda 100 \mu\text{m}$, is displayed in the bottom panel of Fig. 13. At times close to minimum mass loss rate the intensity distribution shows a local maximum at a distance of about $2 \cdot 10^{17}$ cm from the central star. It is much narrower and has a higher intensity contrast than in the case of amorphous carbon. Because our simulations produce lower velocities for the oxygen-rich outflows, the detached dust shell has a higher density and is confined to a smaller width, so it may be more easily detected as a ring-like structure

on a surface brightness map. During the further evolution the position of maximum brightness moves outward at a speed of about 6 km/s while the emission from the detached shell fades away.

5. Comparison with observations

It is presently a widely accepted idea that single carbon stars are formed during the evolution on the AGB when C-rich material is dredged-up from the interior to the O-rich photosphere just after a helium shell flash (Iben & Renzini 1983, Willems & de Jong 1988). The transition from O- to C-rich chemistry could be very fast, taking place on a time scale of the order of years (envelope mixing time). The model proposed by Willems and de Jong assumes that mass loss is strongly reduced, compared to the previous phase of evolution, when the photosphere becomes C-rich for the first time. In consequence, a detached O-rich shell expands away from the visible C-rich star. Up to now 19 carbon

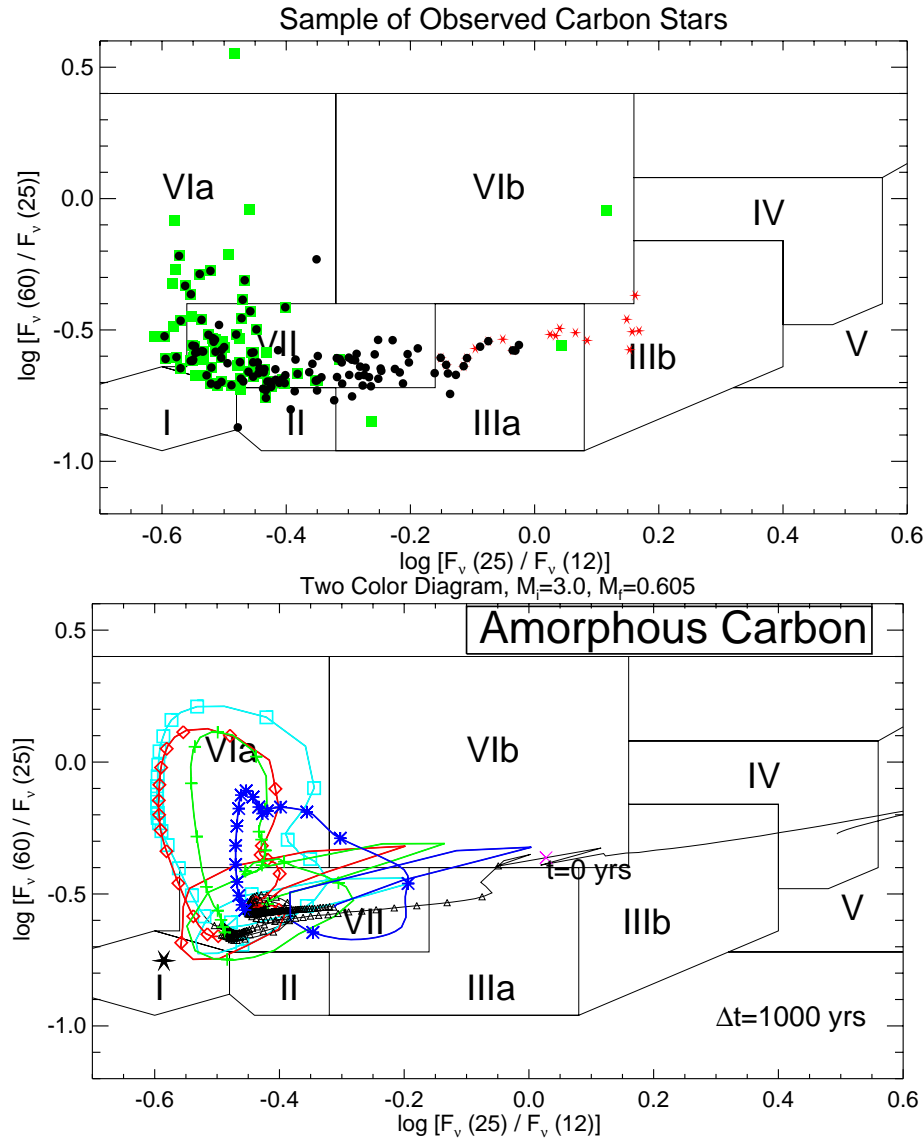


Fig. 14. Top: Distribution of observed carbon stars in the IRAS (60/25 versus 25/12) two-color-diagram. The data for ‘optical’ C stars (classified as C-rich according to their optical spectra; grey squares), ‘classical’ C stars (showing SiC emission at $\lambda 11.3 \mu\text{m}$; black circles), and ‘extreme’ C stars (thick dust shells, central stars not detectable in visual surveys; asterisks) are courtesy of K. Volk (priv. comm.) Only objects with fluxes of quality 3 at 12, 25, 60, and $100 \mu\text{m}$ are plotted. Naturally, there is an overlap between the ‘optical’ and ‘classical’ C stars. **Bottom:** Computed evolution of the standard carbon star model in the same IRAS two-color-diagram, based on the stellar evolution sequence shown in Fig. 2. The hydrodynamical simulation covers four thermal pulses during the final 350 000 years of AGB evolution, each of which produces a corresponding loop in the two-color-diagram, distinguished here by different symbols: squares (B-C), diamonds (D-E), plus-signs (F-G), and asterisks (H-I), plotted at equidistant time intervals of 1000 years, while small triangles are used otherwise (A-B, C-D, E-F, G-H, I-J). The sequence starts somewhere in region VII, reaches the position marked “ $t=0$ ” at the end of the AGB and leaves the diagram to the right when entering the post-AGB phase (the zigzag motion after $t = 0$ is of numerical origin).

rich stars with oxygen-rich envelopes are known (see e.g. Kwok et al. 1997).

Simple modeling (without hydrodynamical effects and with constant mass loss rate) of the O-rich envelopes moving away from the star, performed by Willems & de Jong (1988) and by Chan & Kwok (1988), accounts not only for C stars with silicate dust emission, but also for the optically visible C stars with $60 \mu\text{m}$ excess originating from dust that is too cold to show any signature in the mid-infrared wavelength range. Excess at 60 and/or $100 \mu\text{m}$ is usually interpreted as a signature of a detached shell. In a few cases, re-analysis of IRAS data, observations with ISO or even high-resolution ground-based observations have confirmed the existence of such shells (Waters et al. 1994; Izumiura et al. 1996, 1997; Olofsson et al. 1996).

There is a well known problem with the scenario proposed in the late eighties. Namely, it seems that the detached envelopes around visible carbon stars are rather carbon-rich than oxygen-rich (see e.g. Zuckerman 1993). The estimated life times of C stars is between 10^5 and 10^6 years (e.g. Claussen et al. 1987),

while the life time of a detached shell is about 10^4 years (cf. Figs. 11, 12). Consequently, the fraction of carbon stars with detached shells should be significantly lower than 10% if a mass loss interruption occurs only once at the beginning of the carbon star’s life.

According to the mass loss formula applied in this work, interruption of mass loss happens a few times during the live of a carbon star (assumed here to last at least 350 000 years). Our approach explains in a natural way the observational fact that most of the envelopes around C stars with $60 \mu\text{m}$ excess are carbon rich. Note, however, that we did not consider the transition phase when both sorts of dust (silicate in the outer and carbon in the inner part of the envelope) could co-exist.

5.1. The distribution of AGB stars in the IRAS two-color diagrams

Over the time interval of 350 000 yrs covered by our simulations (Fig. 2), the computed IRAS colors ($F_\nu(25)/F_\nu(12)$),

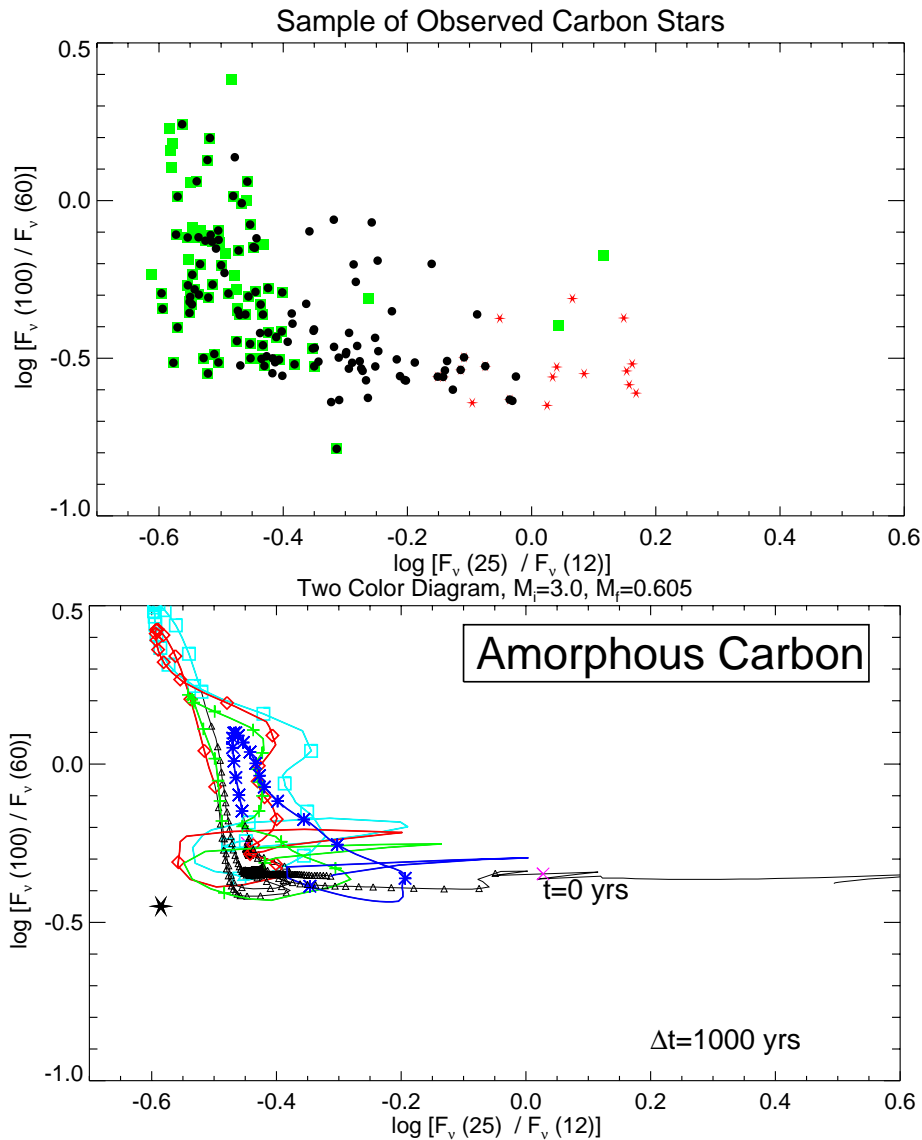


Fig. 15. Same as Fig. 14, but presenting the distribution of observed and computed carbon stars in the IRAS (100/60 versus 25/12) two-color-diagram to include also the 100 μm flux. The big “star” near position (-0.6,-0.45) in the lower diagram represents the black body point for $T = 3000$ K.

$F_{\nu}(60)/F_{\nu}(25)$, $F_{\nu}(100)/F_{\nu}(60)$ vary in correspondence with the dust composition and its distribution inside the shell heated by the central source of radiation. Each of the four thermal pulses produces a distinct loop in the IRAS two-color-diagrams (lower panel of Figs. 14 to 17). The evolutionary behavior of the computed colors can be compared with the distribution of the observational data in the same color-color diagrams (upper panel of Figs. 14 to 17).

From the comparison presented in Figs. 14-17 it is obvious that the problematic co-existence of the both C-based and Si-based dust, as required by Ivezić & Elitzur (1995) in the framework of steady state models, is absolutely not necessary if the time-dependence due to evolutionary changes of the stellar parameters and mass loss rate are taken into account. Our tracks not only cover the areas with observational data but also explain (roughly) the observed relative population densities of the different “cells” in the IRAS two-color-diagrams. Since the theoretical points are plotted at equidistant time intervals (of 1000 years), their number density is a direct measure of the

probability of finding objects in different parts of the diagram. It should be kept in mind, however, that our models are based on a single evolutionary track. Only when the model calculations finally cover a representative sample of initial stellar masses, it will be possible to constrain the variety of proposed mass loss laws from a detailed comparison with observations.

5.1.1. Comparison for carbon stars

In Figs 14 and 15 we compare our theoretical results for the carbon-rich envelope with corresponding observations in two different IRAS color-color diagrams. In Fig 14 the regions introduced by van der Veen & Habing (1988) are shown for reference. The agreement with observational data is quite remarkable in both diagrams.

What is the most important point, Blöcker’s mass loss formula can explain carbon stars with 60 μm excess: The objects located in region VIa (which cannot be understood in the framework of steady state models) are carbon stars just having suf-

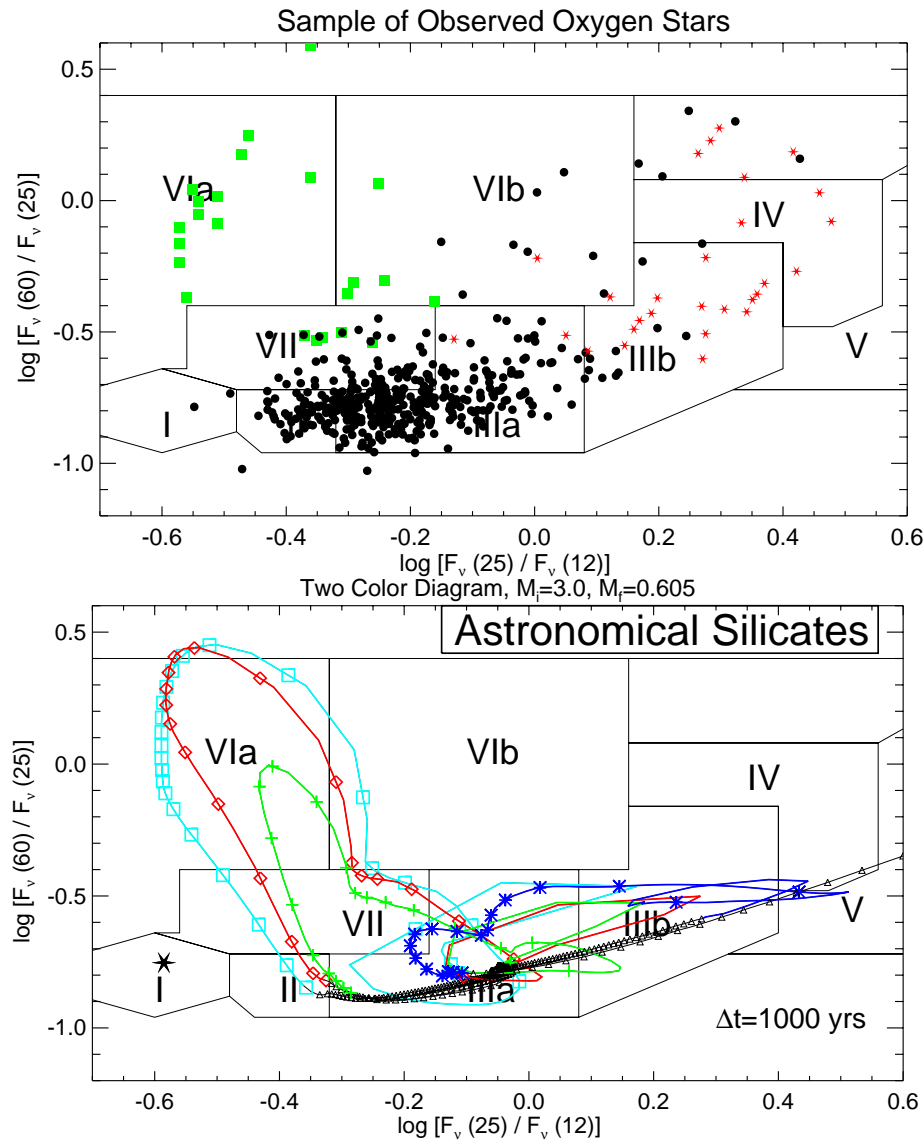


Fig. 16. Top: Distribution of observed oxygen stars in the IRAS (60/25 versus 25/12) two-color-diagram. The data for oxygen stars with silicate emission (black circles) and with silicate absorption (asterisks) are courtesy of K. Volk (priv. comm.); while objects with 60 μm excess (grey squares) are from Zijlstra et al. (1992). Only objects with fluxes of quality 3 at 12, 25, 60, and 100 μm are plotted. **Bottom:** Computed evolution of the standard oxygen star model in the same IRAS two-color-diagram, based on the stellar evolution sequence shown in Fig. 2. As for the carbon star sequence (Fig. 14) the four thermal pulses during the final 350 000 years of AGB evolution lead to four distinct loops in the two-color-diagram (for an explanation of the different symbols see caption of Fig. 14). Again, the time interval between two adjacent symbols is 1000 years. The sequence starts off somewhere in region IIIa, and leaves the diagram to the right at the end of the AGB evolution.

ferred a thermal pulse and are presently in the middle of the subsequent phase of “mass loss interruption” (cf. Willems & de Jong, 1988; Chan & Kwok, 1988) with mass loss rates reduced by at least an order of magnitude.

The only C stars which cannot be readily explained by our models are the extreme C stars (marked by asterisks in Figs. 14 and 15). As has been suggested by Volk et al. (1992), those stars are probably near the end of the AGB evolution and are characterized by huge mass loss. However, our models with amorphous carbon cannot explain their positions in the IRAS two-color diagrams even for mass loss rates as high as $10^{-4} M_{\odot} \text{yr}^{-1}$.

We suggest that the extreme C stars could be explained by the presence of graphite grains, which have a very broad feature around 30 μm (Draine & Lee, 1984, see also Fig. 1 of Paper I). This feature, contributing to the 25 μm IRAS band, would shift our tracks to redder colors. Graphite grains would also explain a slight disagreement in the $F_{\nu}(100)/F_{\nu}(60)$ color seen in Fig. 15, because the extinction cross section of graphite decreases more steeply with wavelengths than for amorphous carbon, so this

color would become slightly bluer, resulting in a better agreement with the observational data. Possibly, the structure of the circumstellar dust grains changes from amorphous to more ordered forms at the highest mass loss rates.

5.1.2. Comparison for oxygen stars

In Figs. 16 and 17, a similar comparison has been performed between oxygen-rich stars and models based on dust composed of “astronomical” silicates. It is now established from observations that mass loss is subject to interruptions also in the case of O-rich stars (Zijlstra et al. 1992). As a natural consequence of such mass loss variability, detached shells are expected to develop repeatedly (not only once during the transition from oxygen-rich to carbon-rich surface composition). Agreement between our track and the observational data in Fig. 16 is fairly good, with the exception of the oxygen-rich stars with silicate absorption (marked by asterisks). However, as has been already shown by Bedijn (1987), O-rich stars in the upper part of regions IIIb and

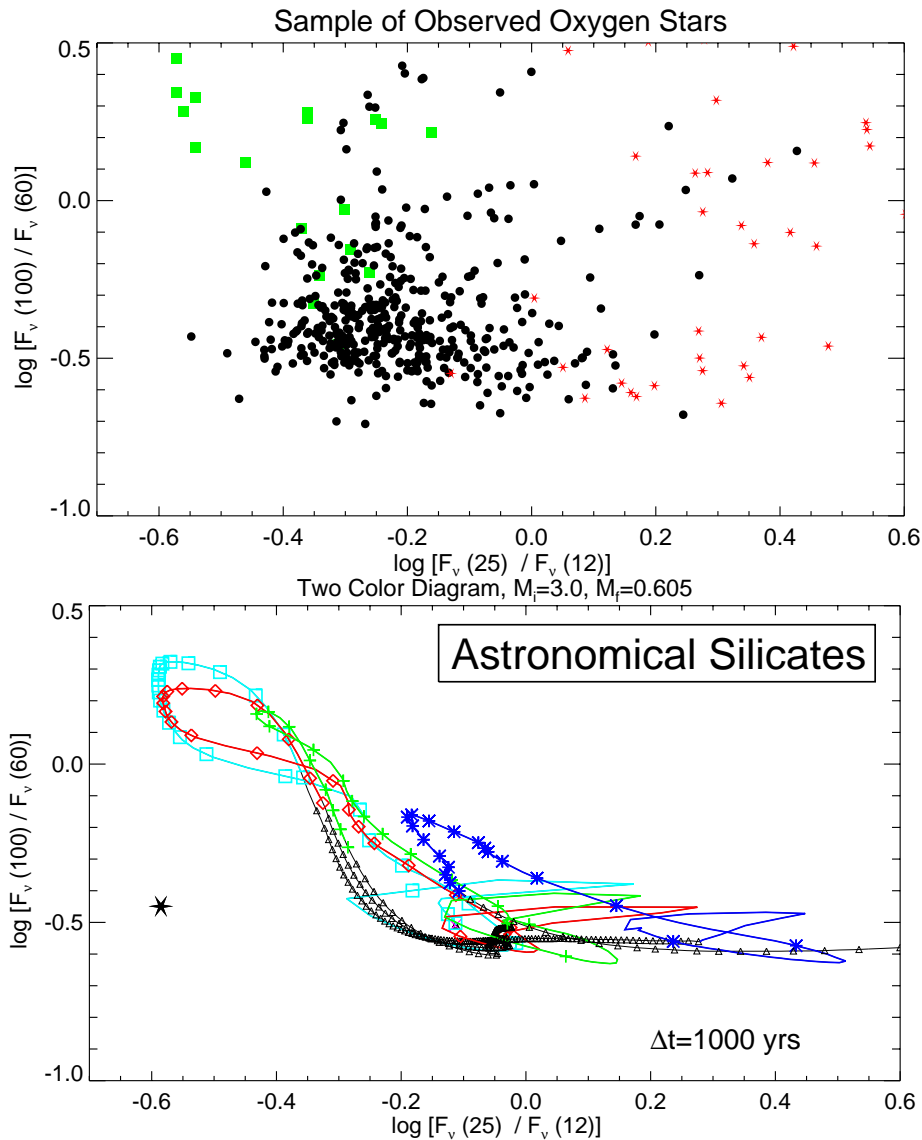


Fig. 17. Same as Fig. 16, but presenting the distribution of observed and computed oxygen stars in the IRAS (100/60 versus 25/12) two-color-diagram. Again, the big “star” near position (-0.6,-0.45) in the lower diagram represents the black body point for $T = 3000$ K.

IV require different dust properties to be explained. Namely, for wavelengths longer than about $30 \mu\text{m}$, the absorption coefficient should decrease less steeply with wavelength than it does in the case of “astronomical” silicates.

Again stars with $60 \mu\text{m}$ excess are pretty well explained by mass loss reduction associated with the decline of luminosity after the helium shell flash. Note, that the predicted time scales agree quite well with the observed density of data points.

Some of the observational points in region VIb might actually be more massive O-rich supergiants moving off the giant region with reduced mass loss. They should be removed from this sample of AGB stars once identified.

In the $F_\nu(25)/F_\nu(12)$ versus $F_\nu(100)/F_\nu(60)$ diagram (Fig. 17) the situation is somewhat worse. While stars with detached shells are still quite well explained by our models, there is a lot of data points in the upper part of diagram. These objects showing silicate emission (probably) cannot all be due to contamination with massive O-rich supergiants.

To understand the situation for these stars with silicate emission, we should point out that O-rich stars are somewhat less evolved than carbon stars. They are therefore somewhat less luminous and have lower mass loss rates, implying smaller $100 \mu\text{m}$ fluxes on average. In consequence, contamination from the cirrus emission could be more severe in this case, resulting in potentially spurious $100 \mu\text{m}$ fluxes.

Again, changes in the optical properties of silicates as proposed by Bedijn (1987) would better explain the observed positions of stars with silicate absorption ($F_\nu(100)/F_\nu(60)$ will increase).

5.1.3. The influence of f_{cond}

As is to be expected, the photometric properties derived from our dynamical models depend somewhat on the assumed dust condensation efficiency f_{cond} . A test calculation for the carbon star sequence with $f_{\text{cond}} \equiv 1$, but otherwise identical parameters, revealed that the loop corresponding to the ‘first’ thermal

pulse (cf. lower panel of Fig. 14), remains almost unchanged, while the amplitude of the ‘second’ and ‘third’ loop is reduced by about a factor of 2. The last loop is again identical. The latter coincidence is easily explained because, for the last loop, $f_{\text{cond}} = 1$ was also valid for the original sequence and we have already seen that the choice of f_{cond} has no significant influence on the dynamics of the outflow. The close agreement of the ‘first’ loop is explained by the fact that during the “mass loss interruption” after the ‘first’ thermal pulse, the density of hot dust in the inner shell is not sufficient to produce significant thermal emission: the flux at 12 and 25 μm is totally dominated by the stellar radiation. A further reduction of the dust density ($f_{\text{cond}} < 1$) does not make any difference. Of course, the “old” dust seen at $\lambda 60 \mu\text{m}$ is also identical since it was produced at times of high mass loss when $f_{\text{cond}} = 1$. Together, this implies that one may expect extended loops to correspond to the previous thermal pulses (not covered by our simulation). For the subsequent thermal pulses, however, the minimum mass loss rate lies at increasingly higher levels (cf. Fig. 2) and the dust emission at 12 and 25 μm is no longer negligible. This explains why the shape and extent of the ‘second’ and ‘third’ loop depends on the choice of f_{cond} .

5.2. The spectral energy distribution of S Scuti

Observationally, several objects with excess dust emission around 60 to 100 μm are known to have well-detached shells (e.g. Olofsson et al. 1996). A prominent example is the well-studied carbon star S Scuti (cf. Groenewegen & de Jong 1994). We selected one post-flash hydrodynamical model from our standard carbon star sequence which comes closest to the observed spectral energy distribution of S Scuti at 60 and 100 μm (see top panel of Fig. 18). Obviously, the model is somewhat too hot to fit the observed fluxes at UV, visual and near infrared wavelengths. At this instant, the model’s central star has an effective temperature of $T_{\text{eff}} \approx 3700 \text{ K}$.

In order to obtain a better overall fit, we have computed another sequence with T_{eff} reduced by 25% relative to the original track, keeping the stellar luminosity unchanged (the stellar radius increases accordingly) as well as retaining the dust properties and numerical parameters. Somewhat surprisingly, we found the dynamics of the circumstellar matter to be considerably affected: the outflow velocity is markedly reduced and the density correspondingly enhanced. Obviously, the efficiency of the radiative dust acceleration is reduced significantly because the cooler central star radiates fewer photons at shorter wavelengths where the dust absorption cross section is largest. Although the wind velocity is now unrealistically low, the enforced time variation of the mass loss rate Fig. 10 again leads to the development of detached dust shells and corresponding excess emission at 60 and 100 μm .

For this sequence, the observed spectral energy distribution is matched most closely at time $t = -203\,115 \text{ yrs}$, when $T_{\text{eff}} = 2770 \text{ K}$, $L_* = 3300 L_{\odot}$ (model SS2, dot-dashed line in the top panel of Fig. 18). The agreement is quite remarkable even though we have not fine-tuned the model to fit this particular

object. Clearly, the model could have been improved by adjusting the stellar parameters, the dust-to-gas ratio and the dust size distribution. Remaining differences in the UV will probably disappear when using a realistic stellar flux distribution instead of assuming a black body spectrum. This is, however, not the purpose of the present work.

For completeness, we show in the bottom panel of Fig. 18 the emergent intensity at different wavelengths ($\lambda 12, 25, 60$, and 100 μm) as a function of the impact parameter for model SS2. We note that a detached dust shell is clearly visible at all wavelengths, unlike the situation shown in the top panel of Fig. 13, but very similar to the model of the oxygen-rich dust shell displayed in the bottom panel of Fig. 13. Obviously, the outflow velocities in the wind of the cool carbon star are comparable to those in the oxygen star with the original (higher) T_{eff} .

5.3. The detached dust shell of Y CVn

In the previous section we have seen that, around the time of minimum mass loss rate, the computed radial intensity distribution shows a local maximum at distances of a few 10^{17} cm from the central star, corresponding to a ring-like structure in the surface brightness (lower panel of Fig. 18). The computed intensity maps show the ring-like structure to be most prominent in the far infrared, $\lambda \approx 100 \mu\text{m}$. Indeed, such detached dust shells have been detected by IRAS (Waters et al. 1994; Izumiura et al. 1997) and by ISO (Izumiura et al. 1996).

In an earlier publication (Steffen & Szczerba 1997), we have compared the radial intensity distribution at $\lambda 100 \mu\text{m}$ computed from hydrodynamical model SS2 (see Sect. 5.2) with the surface brightness map of the carbon star Y CVn obtained at $\lambda 90 \mu\text{m}$ with the ISOPHOT camera on board the *Infrared Space Observatory* (ISO) by Izumiura et al. (1996). The comparison with the synthetic data shows a remarkable qualitative agreement (for details see Fig. 6 of Steffen & Szczerba 1997). In both cases the signature of a *detached dust shell* is clearly discernible as a local maximum in the brightness distribution. In the model the shell’s emission peaks near $r \approx 3 \cdot 10^{17} \text{ cm}$ where the dust temperature is $T_{\text{d}} \approx 50 \text{ K}$.

5.4. Transition to the post-AGB phase: IRAS 17437+5003

Observationally, the end of the AGB evolution is characterized by an optically thin dust shell with a somewhat hotter stellar remnant shining through. Obviously, the mass loss rate must have dropped by orders of magnitude on a very short time scale. The physical reasons for this rapid decline of mass loss, however, are yet unknown. In the empirical mass loss modeling by Blöcker (1995) the rate is coupled to the period of the fundamental radial pulsational mode, P , forcing the transition from the high AGB rate to the much lower Reimers rate (Reimers 1975) to occur between periods of $P = 100$ and 50 days. It happens that this procedure leads to a mass loss reduction of about two orders of magnitude within 100 years (cf. Fig. 2 and top panel of Fig. 19).

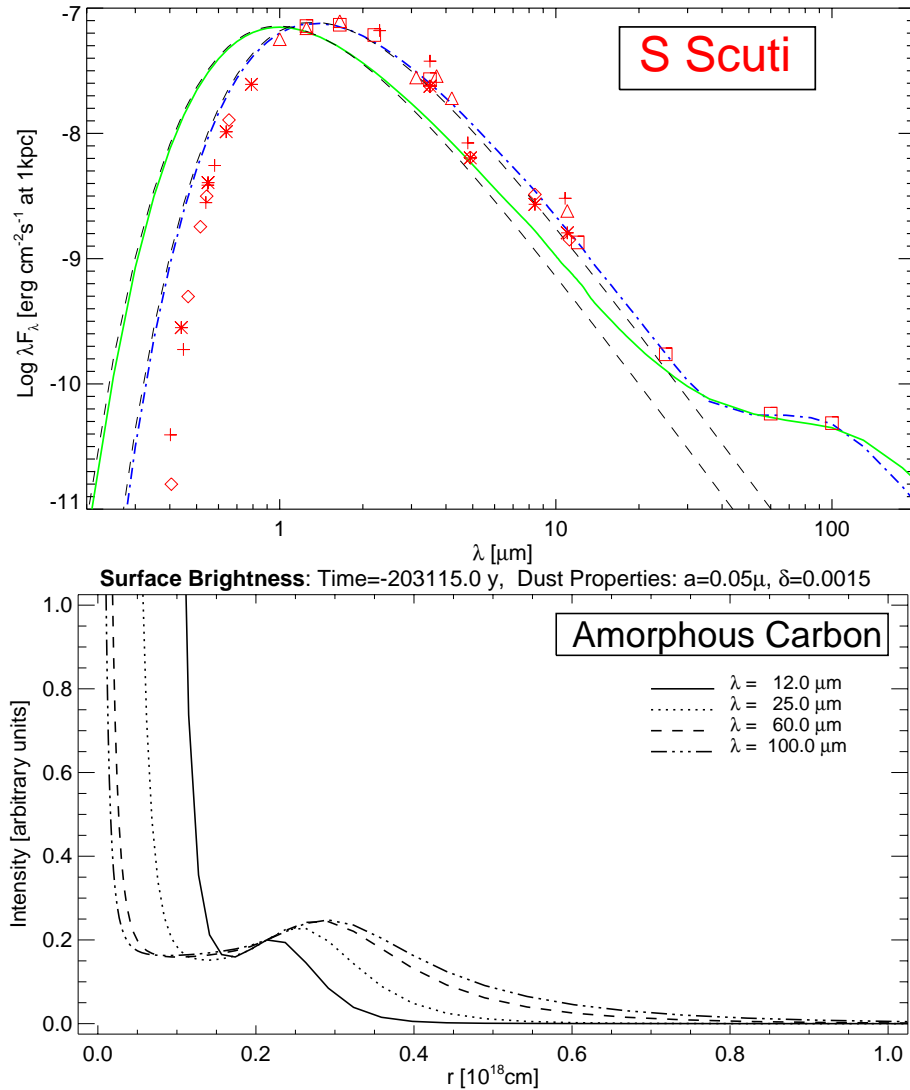


Fig. 18. Top: Observed spectral energy distribution of the well-known carbon star S Scuti (different symbols; data from Groenewegen & de Jong, 1994) compared with two different theoretical spectra. The first one (solid grey, model SS1) is taken from the model sequence shown in Fig. 11 at time $t = -212677$ yrs (close to t_5) such that the model spectrum fits the fluxes at 60 and 100 μm . The corresponding dashed line shows the assumed input spectrum of the AGB star at the center of the detached dust shell, a blackbody with $T_{\text{eff}} = 3700$ K, $L_* = 3400 L_{\odot}$. The second spectrum (dot-dashed, model SS2) is taken from a similar sequence which was computed with T_{eff} reduced by 25% relative to the original track. The optimum fit is obtained at time $t = -203115$ yrs, when $T_{\text{eff}} = 2770$ K, $L_* = 3300 L_{\odot}$. The remarkable agreement with the observed spectral energy distribution is a natural result of the temporal variation of the mass loss rate seen in Fig. 10. Remaining differences in the UV may disappear when using a realistic stellar flux distribution instead of assuming a black body spectrum (corresponding dashed line). **Bottom:** Emergent intensity at λ 12, 25, 60, and 100 μm as a function of impact parameter for model SS2. Intensity is in arbitrary units, normalized to be identical for all wavelengths at $r = 2 \cdot 10^{17}$ cm. A detached dust shell is clearly visible at all wavelengths.

Note that the zero point of our time scale is defined such that $P(t = 0) = 50$ d.

As mentioned in Sect. 4.1.3, we have extended our hydrodynamical simulations several hundred years into the post-AGB regime, using the mass loss law shown in the upper panel of Fig. 19. Indeed we find a rapid detachment and thinning of the dust shell as the density of the newly formed hot dust decreases sharply at the end of the AGB evolution (due to the largely reduced mass loss rate and the sharply increasing dust drift velocity) and gives no detectable signature. The time evolution of the dust density in the inner parts of the shell during the transition to the post-AGB phase is shown in the middle panel of Fig. 19. The rapid depletion of the inner dust shell, caused by the sudden drop of the mass loss rate near $t = 0$, is clearly seen. Note also that the outer parts of the actual dust density profile are considerably steeper than suggested by the r^{-2} density law indicated by the dotted reference line, a consequence of the steadily increasing mass loss rate near the tip of the AGB. The mass loss minimum after the final helium shell flash, centered at $t \approx -30000$ yrs (top panel of Fig. 19) gives rise to a deep local

minimum of the gas density located near $r = 10^{18}$ cm at the beginning of the post-AGB evolution (middle panel of Fig. 19).

The corresponding changes of the emergent spectral energy distribution are illustrated in the bottom panel of Fig. 19 for a simulation based on silicate dust grains. During the covered time interval of about 570 yrs, the strong silicate absorption feature near 10 μm is seen to disappear rapidly with advancing shell detachment, while the thermal emission of the dust becomes progressively more concentrated at far infrared wavelengths. At the same time, the previously totally enshrouded AGB remnant becomes visible, giving rise to a characteristic double-peaked energy distribution. The synthetic spectrum computed for time $t \approx +250$ yrs shows a stunning agreement with the observed spectral energy distribution of the well-known post-AGB object IRAS 17436+5003 = HD 171 796. The comparison is presented in Fig. 20. In principle, the very good agreement of observed and computed spectral energy distribution indicates that the observed relation between the evolution time scale of the star and the detachment time scale of its circumstellar envelope is basically matched by theory. This implies that the mass loss formula

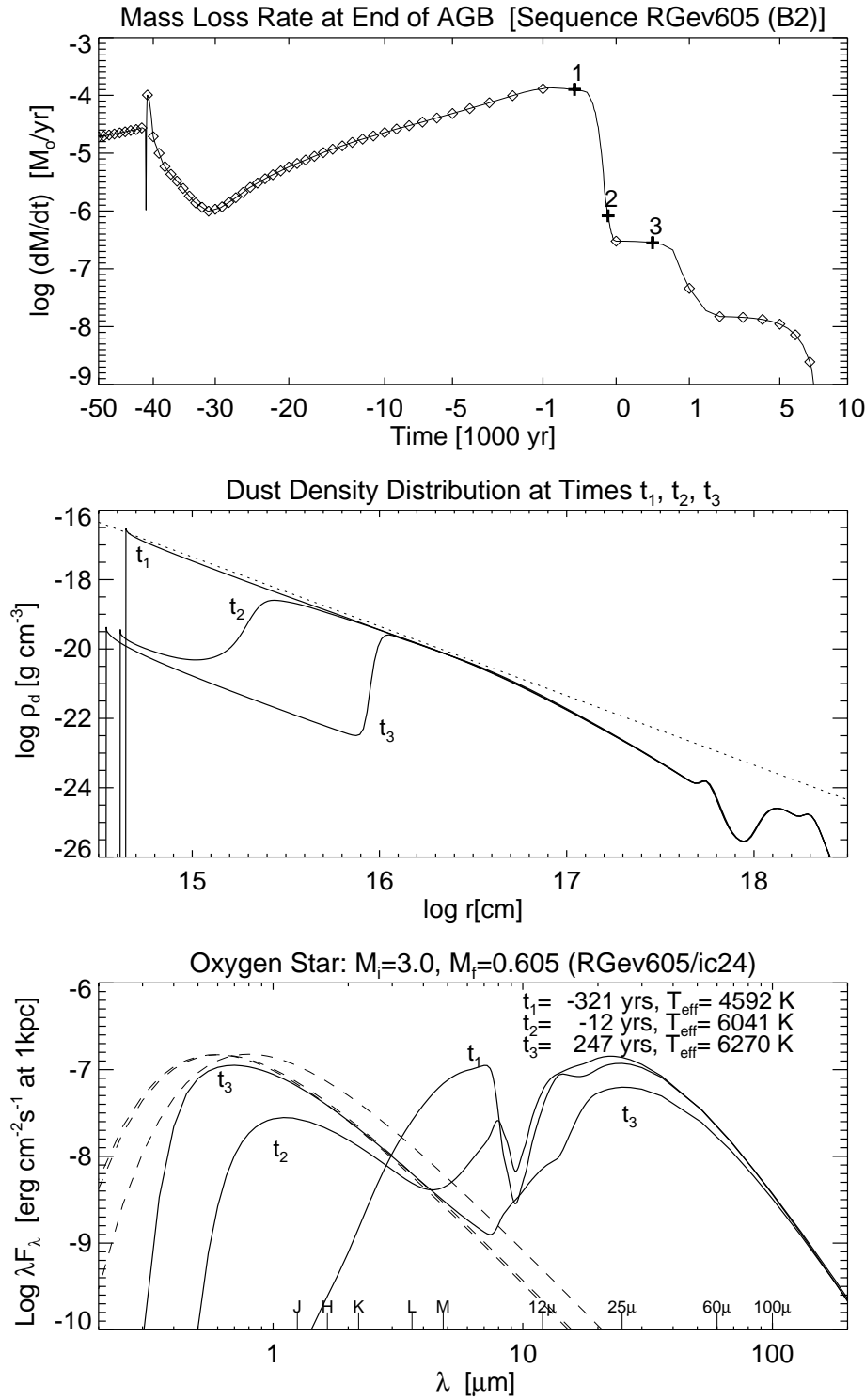


Fig. 19. **Top:** Mass loss rate adopted during the transition from the AGB towards higher effective temperatures (blow-up of rightmost part of Fig. 2, using a *non-linear time-axis* to resolve details near $t=0$). **Middle:** Radial distribution of the dust density at 3 selected times indicated in the upper panel (t_1, t_2, t_3) as obtained from the sequence computed with dust grains composed of “astronomical” silicates. The outer parts of the dust density profile are considerably steeper than suggested by the r^{-2} density law indicated by the dotted reference line. **Bottom:** Corresponding emergent spectral energy distributions (solid lines) at times t_1, t_2, t_3 . The dashed lines indicate the corresponding intrinsic spectra of the central star, for which the effective temperatures are given in the legend.

adopted for the end of the AGB evolution and the wind velocities predicted by our model closely reflect the actual situation.

Finally, in the top panel of Fig. 21, we compare the radial distribution of the *gas* density obtained from the sequences with amorphous carbon dust and with dust of “astronomical” silicates, respectively, at the beginning of the post-AGB phase (about 50 and 150 yrs after the end of the AGB evolution). The outward motion of the inner edge of the gas shell, caused by the

sudden drop of the mass loss rate near $t = 0$, over the considered time interval of 100 yrs is clearly seen. The differences between the carbon-based and the silicate-based models in the inner part of the shell are caused by the different outflow velocities. We have mentioned before (Sect. 4.2) that the radiation pressure on silicate grains is less efficient than for grains of amorphous carbon and hence the outflow velocities are lower for oxygen-rich dust shells. This can also be seen in the lower panel of Fig. 21.

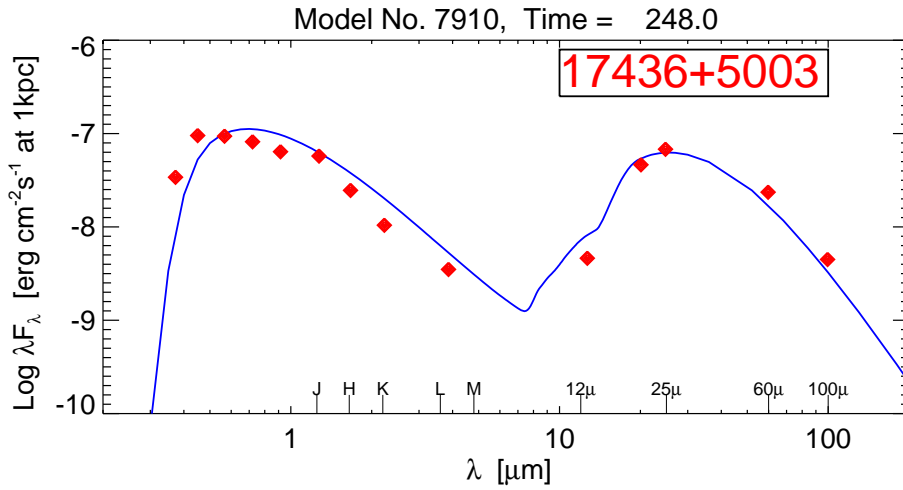


Fig. 20. Spectral energy distribution at time t_3 (solid, also shown in the bottom panel of Fig. 19) compared with observed fluxes of *IRAS* 17436+5003 = HD 161 796 (diamonds; data from Hrivnak et al. 1989). Note that the observations seem to indicate this object to be slightly hotter ($T_{\text{eff}} \approx 7000$ K) than the central star of the model ($T_{\text{eff}} \approx 6300$ K) which, however, was not designed to fit this particular post-AGB star!

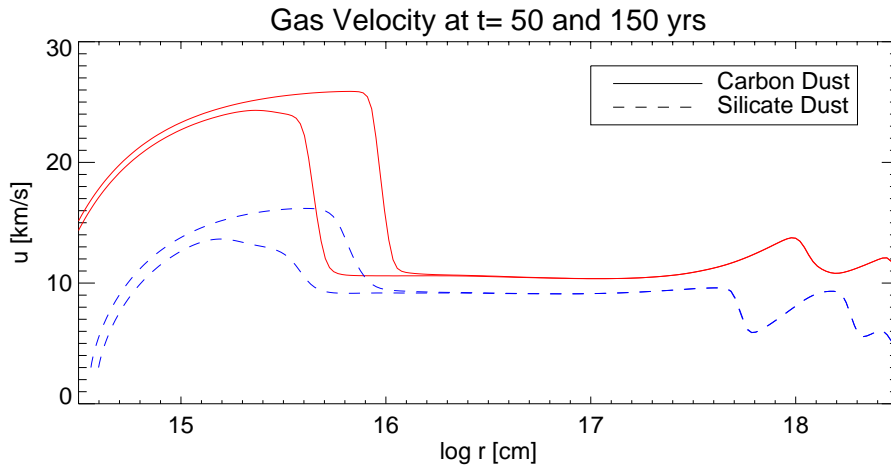
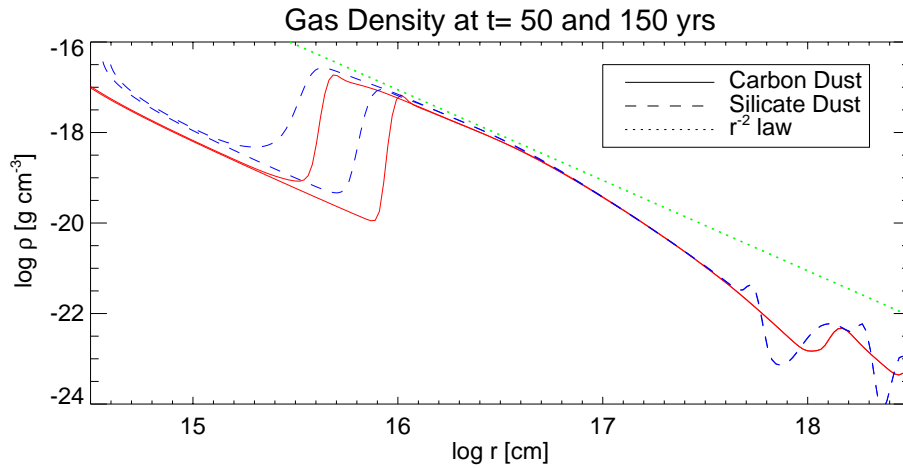


Fig. 21. Top: Radial distribution of the gas density about 50 (left-) and 150 yrs (right-shifted curves) after the end of the AGB evolution as obtained from the sequences with amorphous carbon dust (solid) and with dust of “astronomical” silicates (dashed), respectively. The outward motion of the inner edge of the gas shell, caused by the sudden drop of the mass loss rate near $t = 0$, over the considered time interval of 100 yrs is clearly seen. Note that the actual gas density drops considerably faster with radial distance than suggested by the r^{-2} density law indicated by the dotted reference line. **Bottom:** Similar comparison for the gas velocities.

Over the main parts of the shell, however, the density structure is very similar for both type of models. As was seen for the dust density before (middle panel of Fig. 19), the actual gas density also drops considerably faster with radial distance than $\rho \sim r^{-2}$, reflecting the mass loss history during the previous 50 000 years of evolution.

The density and velocity structure shown in Fig. 21 constitute the starting point for the subsequent development of a planetary nebula. The data are ideally suited as initial conditions for the hydrodynamical modeling of planetary nebulae and have already been used successfully for this purpose (Schönberner et

al. 1997, 1998). The results will be the subject of a more detailed discussion in a forthcoming paper.

6. Concluding remarks

Based on the hydrodynamics simulations presented in this work we have been able to explain the development of large detached dust shells and the corresponding loops in an IRAS two-color diagram as a natural consequence of long-term mass loss variations within a thermal pulse cycle of the central stellar object. Despite the fact that our simulations are only made for one particular AGB evolutionary track, we found very encouraging similarities with the observations existing so far. This is particularly true for the properties of the spectral energy distributions and the appearance of spatially resolved images of carbon stars with detached dust shells.

Although, in principle, a short mass loss “eruption” of sufficient strength and duration could also explain the existence of AGB stars with excess far infrared (FIR) emission, we have shown that for the mass loss law used in the present investigation, the short mass loss spikes associated with the helium shell flashes are *not* the reason for the formation of detached shells in our models. Their amplitude and duration is much too small. Likewise, interaction of the AGB wind with the interstellar medium turns out to be of minor importance in this context. Rather, high mass loss sustained for several ten thousand years, interrupted by extended minima with mass loss rates reduced by orders of magnitude (after a thermal pulse) produces the strong FIR excess and corresponding loops in the IRAS two-color diagram.

We conclude from our hydrodynamical simulations that the density enhancement generated by a short mass loss “eruption” broadens considerably as it moves towards the outer regions of the circumstellar shell due to the existence of substantial velocity gradients. It is therefore not considered as a likely cause for the observed very thin detached CO shells. However, the same simulations provide another mechanism creating thin shells of enhanced gas density, namely the *interaction of winds* of different velocity and density. Once the critical mass loss rate is exceeded, the “dust-driven”, faster wind in the inner parts of the shells runs into the slower “shock-driven” wind in the outer parts, acting like a snow plow piling up matter in a thin shell at the interface between both type of winds (for details see Steffen & Schönberner 1998).

It should be noted that the models discussed here are far from being fully self-consistent: they cover only those parts of the circumstellar envelope that lie outside the sonic point and therefore cannot make predictions about the mass loss rate which depends on the conditions close to the stellar surface. Fully self-consistent theoretical models of circumstellar AGB shells require the incorporation of stellar pulsations, dust chemistry, multi-component hydrodynamics and stellar evolution.

While we do not intend to take up such an ambitious project, we plan several smaller steps to improve our model calculations for future applications. These include introducing a *distribution of grain sizes*, developing *improved formulae for f_{cond} and*

g_{shock} based on more physical models, and the incorporation of an *energy equation for the gas component*. Based on the resulting improved models, CO dissociation and line formation computations could be performed to study the problem of the origin of thin detached CO shells in more detail.

Acknowledgements. We are indebted to H. Yorke for the permission to modify his original code and to apply it to the problem of dusty stellar outflows. We thank T. Blöcker for providing us with the data from his stellar evolution calculations with mass loss. Part of this research is funded by “Deutsche Agentur für Raumfahrtangelegenheiten (DARA) under grant 50 OR 9411. One of us (R. Sz.) expresses his gratitude to the Canadian Institute of Theoretical Astrophysics, to the Astrophysical Institute Potsdam, and to the Polish State Committee for Scientific Research - grants No. 2.P03D.027.10 and 2.P03D.002.13. M.S. gratefully acknowledges the the hospitality and support provided by the Nicolaus Copernicus Astronomical Center, Torun.

References

- Arndt, T.U., Fleischer, A.J., Sedlmayr, E. 1997, A&A 327, 614
 Bedijn, P.J. 1987, A&A 186, 136
 Blöcker, T. 1995, A&A 297, 727
 Bowen, G.H. 1988, ApJ 329, 299
 Chan, S.J., Kwok, S. 1988, ApJ 334, 362
 Claussen, M.J., Kleinmann, S.G., Joyce, R.R., Jura M. 1987, ApJS 65, 385 AJ 107, 1469
 Dominik, C., Gail, H.-P., Sedlmayr, E., Winters, J.M. 1990, A&A 240, 365
 Draine, B., Lee, H.M. 1984, ApJ 285, 89
 Egan, M.P., Kwok, S., Leung, C.M., Price, S.D. 1996, A&A 308, 738
 Gilman, R.C. 1972, ApJ 178, 423
 Goldreich, P., Scoville, N. 1976, ApJ 205, 144
 Groenewegen, M.A.T., de Jong, T. 1994, A&A 282, 115
 Habing, H.J., Tignon, J., Tielens, A.G.G.M. 1994, A&A 286, 523
 Herman, J., Burger, J.H., Penninx, W. 1986 A&A 167, 247
 Hrivnak, B.J., Kwok, S., Volk, K. 1989, ApJ 346, 265
 Iben, I., Renzini, A. 1983, ARA&A 21, 271
 Ivezić, Z., Elitzur, M. 1995, ApJ 445, 415
 Izumiura, H., Hashimoto, O., Kawara, K., Yamamura, I., Waters, L.B.F.M. 1996, A&A 315, L221
 Izumiura, H., Waters, L.B.F.M., de Jong, T., et al. 1997, A&A 323, 449
 Jura, M. 1987, ApJ 313, 743
 Knapp, G.R., Morris, M. 1985, ApJ 292, 640
 Kwok, S. 1975, ApJ 198, 583
 Kwok, S., Volk K., Bidelman W.P. 1997, ApJS 112, 557
 Laor, A., Draine, B.T. 1993, ApJ 402, 441
 Netzer, N., Knapp, G.R. 1987, ApJ 323, 734
 Olofsson, H., Bergman, P., Eriksson, K., Gustafsson, B. 1996, A&A 311, 587
 Olofsson, H., Bergman, P., Lucas, R., et al. 1998, A&A 330, L1
 Reimers, D. 1975, in *Problems in Stellar Atmospheres and Envelopes*, eds. B. Baschek, W.H. Kegel, G. Traving, Springer-Verlag, Berlin, p. 229
 Rouleau, F., Martin, P.G. 1991, ApJ 337, 526
 Salpeter, E.E. 1974, ApJ 193, 585
 Schönberner, D., Steffen, M., Stahlberg, J., Kifonidis, K., Blöcker, T. 1997, in *Advances in Stellar Evolution*, eds. R.T. Rood and A. Renzini, Cambridge University Press, p. 146
 Schönberner, D., Steffen, M., Stahlberg, J., Kifonidis, K., Blöcker, T. 1998, in *The Carbon Star Phenomenon*, Proc. IAU Symp. 177, ed. R.F. Wing, Kluwer Academic Publishers (in press)

- Schutte, W., Tielens, A.G.G.M. 1989, ApJ 343, 369
- Shu, K.-W. 1997, MNRAS 289, 559
- Shu, K.-W., Jones, T.J. 1997, ApJ 479, 918
- Steffen, M., Schönberner, D. 1998, A&A (submitted)
- Steffen, M., Szczerba, R. 1997, Ap&SS 251, 131
- Steffen, M., Szczerba, R., Men'shchikov, A., Schönberner, D. 1997a, A&AS 126, 39
- Steffen, M., Szczerba, R., Men'shchikov, A., Schönberner, D. 1997b, in *Advances in Stellar Evolution*, eds. R.T. Rood and A. Renzini, Cambridge University Press, p. 154
- Szczerba, R., Marten, H. 1993, in *Mass Loss on the AGB and Beyond*, ed. H.E. Schwarz, ESO Conference and Workshop Proceedings No. 46, p. 90
- Vassiliadis, E., Wood, P.R. 1992, Proc. Astron. Soc. Aust. 10 (1), 30
- Vassiliadis, E., Wood, P.R. 1993, ApJ 413, 641
- van der Veen, W.E.C.J., Habing, H.J. 1988, A&A 194, 125
- Volk, K., Kwok, S., Langill, P.P. 1992, ApJ 391, 285
- Waters, L.B.F.M., Loup, C., Kester, D.J.M., Bontekoe, Tj.R., de Jong, T. 1994, A&A 281, L1
- Willems, F.J., de Jong, T. 1988, A&A 196, 173
- Wood, P.R. 1979, ApJ 227, 220
- Yorke, H.W. 1980a, A&A 85, 215
- Yorke, H.W. 1980b, A&A 86, 286
- Yorke, H.W., Krügel, E. 1977, A&A 54, 183
- Zijlstra, A., Loup, C., Waters, L.B.F.M., de Jong, T. 1992, A&A 265, L5
- Zuckerman, B. 1993, A&A 276, 367